Cell Reports

Knockout of the LRRK2-counteracting RAB phosphatase PPM1H disrupts axonal autophagy and exacerbates alpha-synuclein aggregation

Graphical abstract

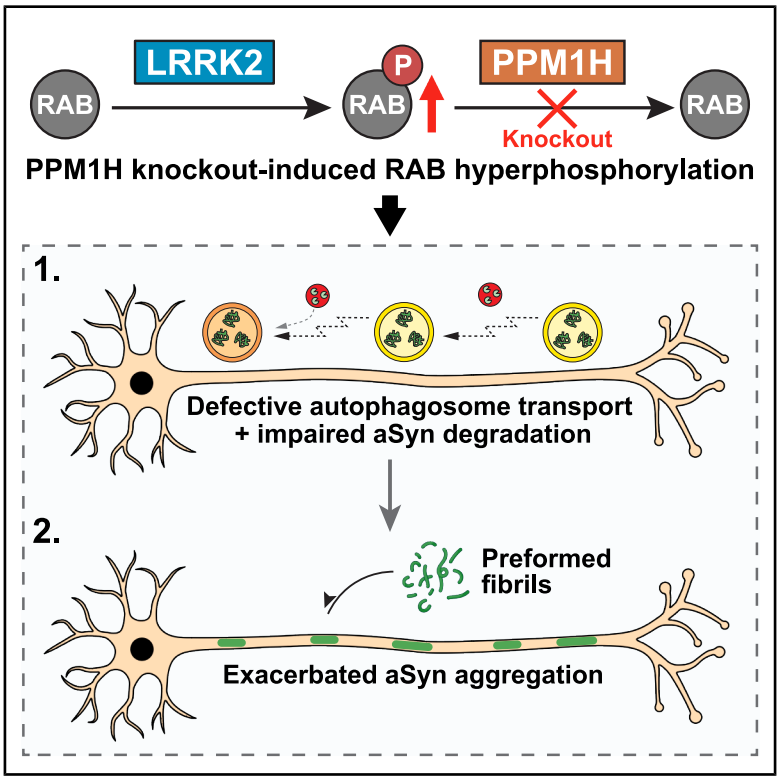

Highlights

- Dysregulated LRRK2-pRAB-PPM1H signaling impairs axonal autophagy
- Loss of PPM1H disrupts axonal autophagosome transport and α-synuclein degradation
- Loss of PPM1H exacerbates α-synuclein aggregation in a LRRK2-dependent manner

Authors

Michel Fricke, Anna Mechel, Lennart Evers, ..., Markus Zweckstetter, Erika L.F. Holzbaur, C. Alexander Boecker

Correspondence

alexander.boecker@med.uni-goettingen.de

In brief

Fricke et al. find that knockout of the RAB phosphatase PPM1H disrupts axonal autophagosome transport, impairs autophagosomal degradation of axonal α-synuclein, and exacerbates PFF-seeded α-synuclein aggregation in a LRRK2-dependent manner, linking dysregulation of the LRRK2-pRAB-PPM1H axis to defective axonal autophagy and α-synuclein pathology.

Fricke et al., 2026, Cell Reports *45*, 117364
June 23, 2026
https://doi.org/10.1016/j.celrep.2026.117364

CellPress

Cell Reports

CellPress
OPEN ACCESS

Report

Knockout of the LRRK2-counteracting RAB phosphatase PPM1H disrupts axonal autophagy and exacerbates alpha-synuclein aggregation

Michel Fricke,[1,8] Anna Mechel,[1,8] Lennart Evers,[1] Björn Twellsieck,[1] Jessica M. Grein,[1] Maria-Sol Cima-Omori,[2] Mohammed Al-Azzani,[3] Tiago F. Outeiro,[2,3,4,5] Markus Zweckstetter,[2,6] Erika L.F. Holzbaur,[7] and C. Alexander Boecker[1,9,*]

[1]University Medical Center Goettingen, Department of Neurology, 37077 Goettingen, Germany
[2]German Center for Neurodegenerative Diseases (DZNE), 37075 Goettingen, Germany
[3]University Medical Center Goettingen, Department of Experimental Neurodegeneration, Center for Biostructural Imaging of Neurodegeneration, 37073 Goettingen, Germany
[4]Faculdade de Medicina e Ciências Biomédicas, Algarve Biomedical Center Research Institute (ABC-Ri), Universidade do Algarve, 8005-139 Faro, Portugal
[5]Translational and Clinical Research Institute, Faculty of Medical Sciences, Newcastle University, NE2 4HH Newcastle upon Tyne, UK
[6]Department for NMR-based Structural Biology, Max Planck Institute for Multidisciplinary Sciences, 37077 Goettingen, Germany
[7]Department of Physiology, Perelman School of Medicine, University of Pennsylvania, Philadelphia, PA 19104, USA
[8]These authors contributed equally
[9]Lead contact
*Correspondence: alexander.boecker@med.uni-goettingen.de
https://doi.org/10.1016/j.celrep.2026.117364

SUMMARY

Parkinson disease (PD)-associated mutations in the *LRRK2* gene hyperactivate LRRK2 kinase activity, leading to increased phosphorylation of a subset of RAB GTPases, which are master regulators of intracellular trafficking. In neurons, processive retrograde transport of autophagosomes is essential for autophagosome maturation and effective degradation of autophagosomal cargo in the axon. Here, we show that knockout of the LRRK2-counteracting RAB phosphatase PPM1H causes a gene-dose-dependent disruption of the axonal transport of autophagosomes, leading to impaired degradation of axonal alpha-synuclein (aSyn), a key protein in PD pathophysiology. Defective autophagosome transport and impaired aSyn degradation correlate with increased aSyn aggregation in primary *PPM1H* knockout neurons exposed to preformed fibrils of aSyn, an effect that is dependent on LRRK2 kinase activity. These findings mechanistically link LRRK2-mediated RAB hyperphosphorylation to defective autophagosomal degradation and enhanced aggregation of aSyn, positioning the LRRK2-RAB axis as a key driver of PD pathophysiology.

INTRODUCTION

Pathogenic mutations in the leucine-rich repeat kinase 2 (*LRRK2*) gene are a major genetic risk factor for Parkinson disease (PD). These mutations induce increased LRRK2 kinase activity, leading to hyperphosphorylation of a subset of RAB GTPases.[1,2] Increased LRRK2 kinase activity and RAB hyperphosphorylation are also induced indirectly by the PD mutations *VPS35*-p.D620N and *RAB32*-p.S71R[3–5] and have been observed upon exposure to PD-causing environmental toxins[6,7] as well as in cases with idiopathic PD.[8] Furthermore, recent reports link inactivating mutations of the LRRK2-counteracting RAB phosphatases PPM1H and PPM1M to PD.[9–11] Taken together, these observations suggest that several causes of PD may converge on a similar core mechanism of elevated LRRK2-mediated RAB phosphorylation. However, it is still unclear how RAB hyperphosphorylation may mediate the neurodegeneration found in patients with PD.

In previous work, we found that increased LRRK2 kinase activity disrupts the axonal transport of autophagic vesicles (AVs) via RAB hyperphosphorylation.[12–14] AVs are primarily formed in the distal axon and at presynaptic sites before undergoing processive dynein-driven retrograde transport toward the soma.[15–18] During retrograde transport, AVs fuse with lysosomes, lowering the intralumenal pH and activating degradative enzymes.[19,20] Importantly, processive AV transport is tightly linked to effective AV maturation and degradative function.[21–23] Hyperactive LRRK2 inappropriately activates competing kinesin motors on the AV, leading to an unregulated tug-of-war that disrupts transport and induces defective maturation of axonal AVs.[12,13] While these findings indicate that LRRK2-dependent RAB hyperphosphorylation perturbs axonal autophagy, it remains unclear whether such defects compromise degradation of disease-relevant autophagosomal cargo and thereby contribute to PD pathogenesis.

Alpha-synuclein (aSyn) is an autophagosomal cargo of particular interest,[24–26] as its aggregation into Lewy bodies and Lewy

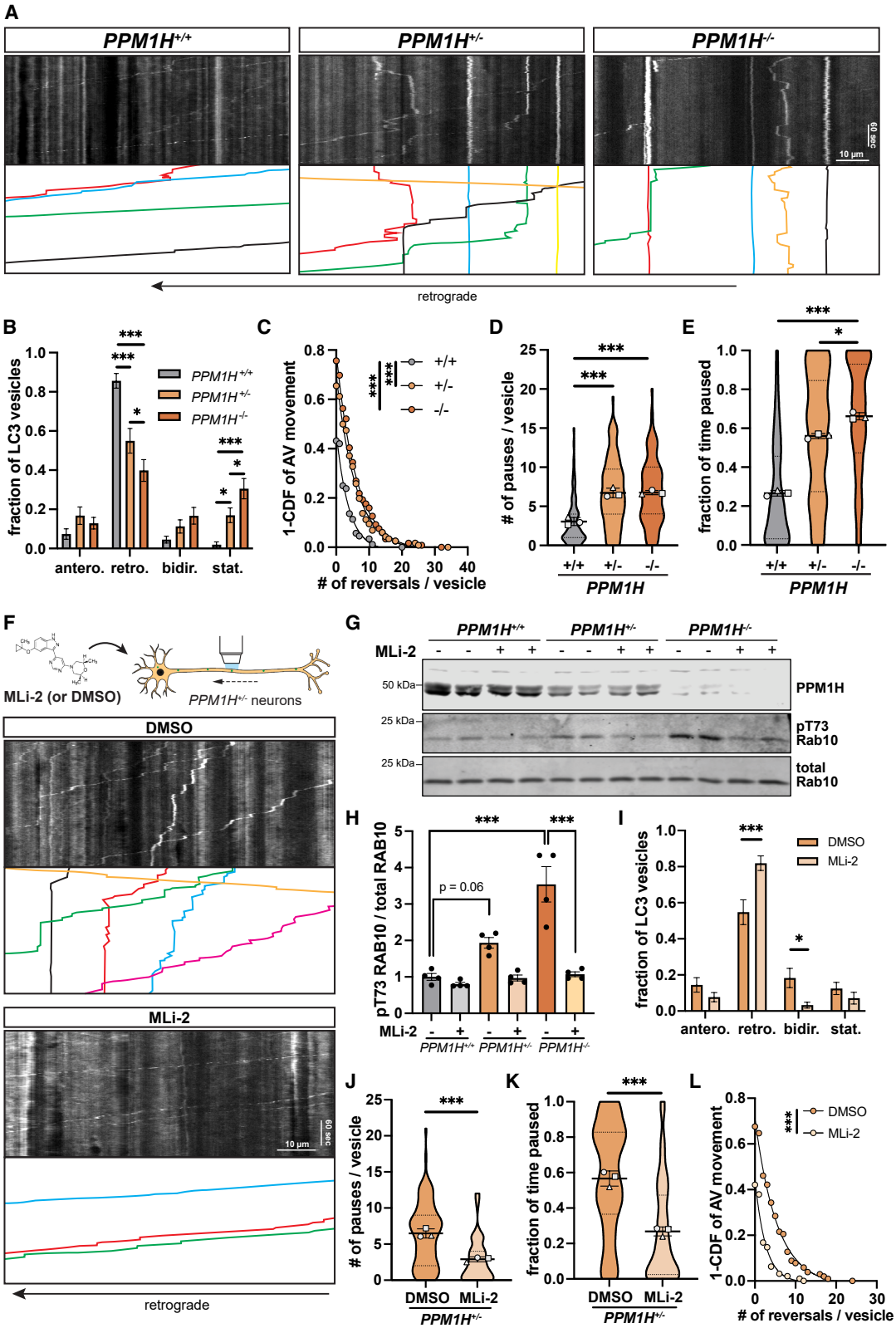

(legend on next page)

neurites is the pathological hallmark of PD and a cardinal feature of PD disease progression. aSyn is predominantly found at presynaptic sites, the primary location of neuronal AV biogenesis.[27] Notably, previous work has shown increased formation of axonal aSyn aggregates following preformed fibril (PFF) treatment in different types of neurons expressing hyperactive LRRK2.[28–32] However, the mechanistic connection between hyperactive LRRK2 and exacerbated aSyn pathology remains unresolved.

Here, we leveraged knockout (KO) models of the LRRK2-counteracting RAB phosphatase PPM1H to investigate whether the effects of pathogenic LRRK2 on aSyn pathology are mediated by RAB hyperphosphorylation. Primary *PPM1H* KO neurons exhibited *PPM1H*-gene-dose- and LRRK2-kinase-activity-dependent defects in retrograde AV transport that were accompanied by impaired autophagosomal degradation of axonal aSyn. These defects in AV transport and cargo degradation correlated with increased aSyn aggregation in *PPM1H* KO primary neurons upon treatment with PFFs, an effect that was rescued by pharmacological LRRK2 kinase inhibition. Together, these findings provide mechanistic evidence linking RAB hyperphosphorylation to disrupted axonal autophagy and increased aSyn aggregation, supporting a central role for the LRRK2-RAB axis in PD pathogenesis.

RESULTS

Knockout of the LRRK2-counteracting phosphatase PPM1H disrupts AV transport in mouse cortical neurons

Loss of the LRRK2-counteracting RAB phosphatase PPM1H was previously determined to disrupt axonal AV transport in human induced pluripotent stem cell (iPSC)-derived $PPM1H^{-/-}$ neurons.[13] To assess whether this phenotype is consistent across different model systems and to test the effect of heterozygous PPM1H loss, we investigated the axonal transport of mScarlet-LC3B-labeled AVs in $PPM1H^{+/+}$, $PPM1H^{+/-}$, and $PPM1H^{-/-}$ primary neurons from *PPM1H* KO mice (Figure 1A).[33] Western blots showed increased levels of LRRK2-phosphorylated pT73 RAB10 in $PPM1H^{-/-}$ neurons and a trend toward increased pT73 RAB10 levels in $PPM1H^{+/-}$ neurons (Figures S1A–S1C). In live imaging experiments, decreased PPM1H expression markedly affected the directionality of axonal AVs by increasing the stationary fraction of AVs at the expense of the retrograde fraction (Figure 1B). The increase in stationary AVs was significantly higher in $PPM1H^{-/-}$ than in $PPM1H^{+/-}$ neurons, suggesting a gene-dose-dependent effect. To further characterize the effect of loss of PPM1H on AV transport, we quantified non-processive motility and pausing behavior of motile AVs. We found that both heterozygous and homozygous *PPM1H* KO resulted in reduced AV processivity compared to $PPM1H^{+/+}$, with a higher number of directional reversals (Figure 1C) and a significant increase in the number of pauses and pause duration (Figure 1D; Figure S1D). This robust increase in non-processive motility and pausing is consistent with the model of an underlying "tug-of-war" between anterograde and retrograde motor proteins that was proposed in previous work.[12,13] Together, the increased pausing of motile AVs and the higher number of stationary AVs resulted in a marked increase in the overall fraction of time that *PPM1H* KO AVs spent in a paused state (Figure 1E). Due to their even higher number of stationary AVs, the overall fraction of time paused was significantly longer in $PPM1H^{-/-}$ neurons than in $PPM1H^{+/-}$ neurons (Figure 1E).

To determine whether the observed transport defects are LRRK2-dependent, we treated primary *PPM1H* KO neurons with the selective LRRK2 kinase inhibitor MLi-2 (Figure 1F).[34] Western blots confirmed that MLi-2 reduced pT73 RAB10 phosphorylation, resulting in levels comparable to those observed in wild-type (WT) neurons (Figures 1G and 1H). For live imaging experiments, we focused on $PPM1H^{+/-}$ neurons, which showed significant impairment of AV transport and were more readily available than $PPM1H^{-/-}$ neurons from breeding heterozygous mice. MLi-2 significantly increased the retrograde fraction of AVs in $PPM1H^{+/-}$ neurons (Figure 1I) and decreased the number of pauses of motile AVs, restoring the overall fraction of time paused to levels similar to untreated $PPM1H^{+/+}$ neurons (Figures 1J and 1K). Non-processive motility, as measured by number of reversals, was also improved by LRRK2 inhibition (Figure 1L).

Together, these findings show that loss of PPM1H disrupts axonal AV transport in primary neurons in a LRRK2-kinase-activity-dependent manner. Homozygous *PPM1H* KO neurons showed a more severe transport impairment than heterozygous *PPM1H* KO neurons, suggesting that the AV transport deficit scales with the extent of RAB hyperphosphorylation by LRRK2.

Figure 1. Knockout of PPM1H in primary neurons disrupts axonal AV transport in an LRRK2-kinase-dependent manner

(A) Kymographs of axonal mScarlet-LC3+ vesicles in $PPM1H^{+/+}$, $PPM1H^{+/-}$, and $PPM1H^{-/-}$ mouse cortical neurons. Example AV traces are highlighted.

(B) Directionality of AVs in *PPM1H* KO neurons. Antero., anterograde; retro., retrograde; bidir., bi-directional; stat., stationary (mean ± SEM; $n = 27–29$ neurons from three independent experiments; $^{*}p < 0.05$, $^{**}p < 0.01$, $^{***}p < 0.001$; two-way ANOVA with Sidak's multiple comparisons test).

(C–E) Directional reversals (C) and pause number (D) of motile AVs, as well as fraction of time paused of all AVs (E) in *PPM1H* KO neurons [$n = 88–119$ motile AVs (C and D) and 90–167 total AVs (E) from 27 to 29 neurons from three independent experiments; $^{*}p = 0.0187$, $^{***}p < 0.001$; mixed effects model analysis].

(F) Kymographs of axonal mScarlet-LC3+ vesicles in $PPM1H^{+/-}$ neurons treated overnight with DMSO or 100 nM MLi-2.

(G and H) Western blot and pT73 RAB10 quantification normalized to total RAB10- and DMSO-treated WT in $PPM1H^{+/+}$, $PPM1H^{+/-}$, and $PPM1H^{-/-}$ mouse cortical neurons treated with DMSO or MLi-2 (mean ± SEM; $n = 4$ biological replicates; ns, not significant; $^{***}p < 0.0006$; one-way ANOVA with Tukey's multiple comparisons test).

(I) Directionality of AVs in $PPM1H^{+/-}$ neurons treated with DMSO or MLi-2 ($n = 23–24$ neurons from three independent experiments; $^{*}p < 0.05$, $^{***}p < 0.001$; two-way ANOVA with Sidak's multiple comparison test).

(J–L) Pause number (J) of motile AVs, fraction of time paused (K) of all AVs, and directional reversals (L) of motile AVs in $PPM1H^{+/-}$ neurons treated with DMSO or MLi-2 [$n = 95–102$ motile AVs (J and L) and 100–118 total AVs (K) from 23 to 24 neurons from three independent experiments; $^{***}p < 0.001$; mixed effects model analysis]. Scatterplot points indicate the means of three independent experiments, and error bars show mean ± SD of these points. For (C and L), curve fits were generated using nonlinear regression (two-phase decay).

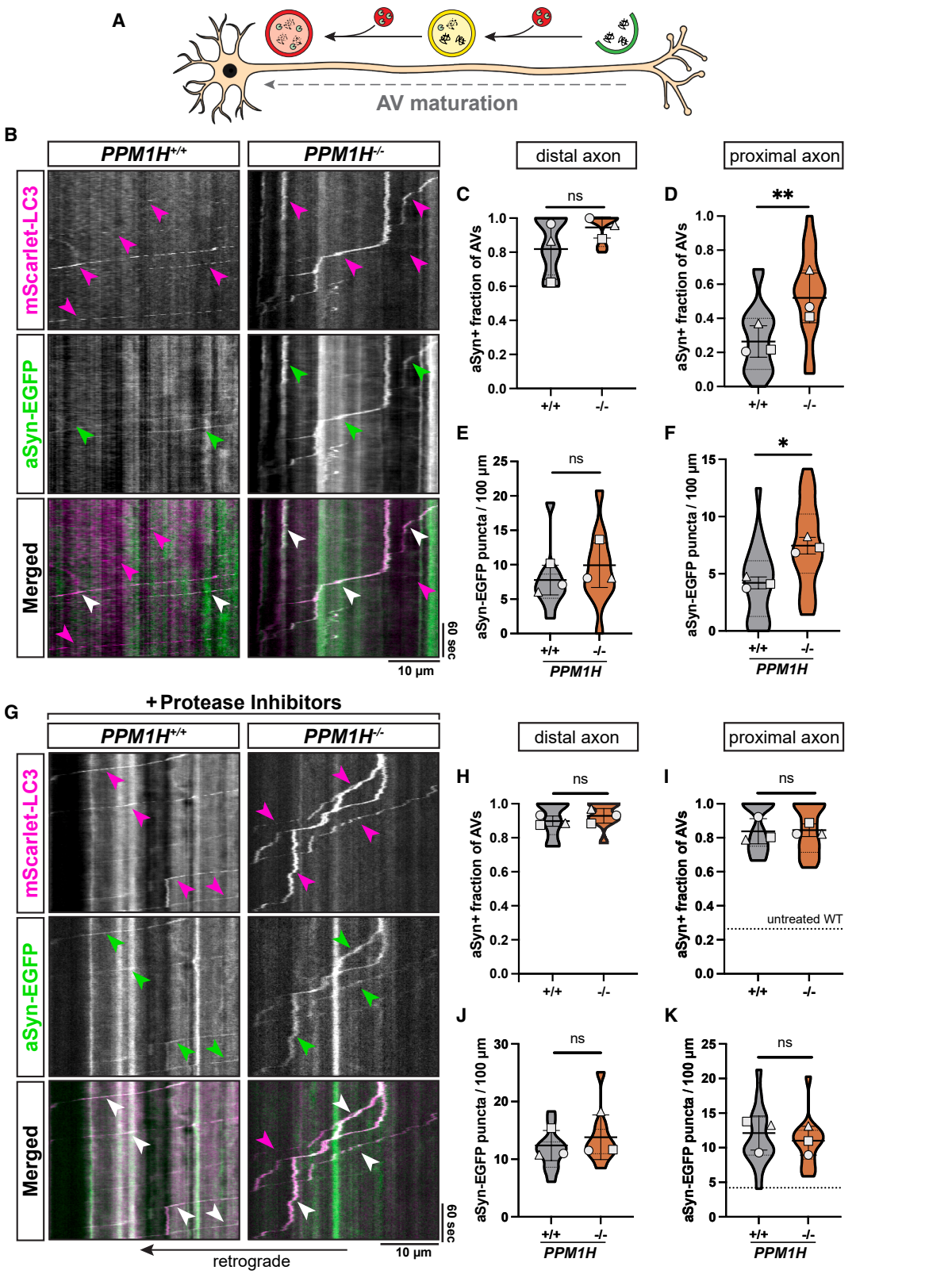

(legend on next page)

Impaired AV transport is associated with defective autophagosomal degradation of aSyn-EGFP

The key PD protein aSyn is an established substrate of autophagy and is enriched at presynaptic sites in the distal axon, the primary location of neuronal AV biogenesis.[24–26] Upon formation in the distal axon, AVs are transported retrogradely toward the cell soma, maturing *en route* by fusion with lysosomal vesicles (Figure 2A).[15–19] Impaired transport has previously been linked to defective maturation of axonal AVs during retrograde trafficking.[12,21,23]

We asked whether disruption of AV transport by *PPM1H* KO affects the autophagosomal degradation of axonal aSyn. To test this, we overexpressed aSyn-EGFP in *PPM1H*$^{+/+}$ and *PPM1H*$^{-/-}$ mouse cortical neurons together with mScarlet-LC3B as an AV marker (Figure 2B). AV density in the distal axon was unchanged, suggesting that *de novo* AV formation is independent of PPM1H (Figure S1E). Approximately 80%–90% of AVs colocalized with aSyn-EGFP in the distal axon of both *PPM1H*$^{+/+}$ and *PPM1H*$^{-/-}$ neurons, indicating that cargo uptake into newly formed AVs was also unaffected (Figure 2C). The proximal axon contained a much lower fraction of aSyn+ AVs (Figure 2D), consistent with the degradation of engulfed aSyn-EGFP during the retrograde transport of maturing AVs (Figure 2A). Notably, the fraction of aSyn+ AVs in the proximal axon of *PPM1H*$^{-/-}$ neurons was significantly higher than in *PPM1H*$^{+/+}$ controls (Figure 2D). This was accompanied by a higher overall density of aSyn-EGFP puncta in the proximal, but not distal, axon (Figures 2E and 2F). Cytosolic aSyn-EGFP levels were comparable across genotypes, excluding differences in expression as a confounding factor (Figure S1F).

Extending these findings to human iPSC-derived neurons, *PPM1H*$^{-/-}$ iNeurons similarly showed a significant increase in the fraction of aSyn+ AVs and a trend toward elevated aSyn-EGFP puncta in the proximal axon (Figures S1G–S1I). Together, these data indicate that PPM1H deficiency impairs autophagosomal degradation of aSyn across model systems, leading to its accumulation in the proximal axon under conditions of overexpression.

To further test whether the observed alterations reflect impaired autophagosomal cargo degradation, we next treated *PPM1H*$^{+/+}$ and *PPM1H*$^{-/-}$ primary neurons co-expressing aSyn-EGFP and mScarlet-LC3 with the lysosomal protease inhibitors pepstatin A and E64d (Figure 2G).[35] In the distal axon, the fraction of aSyn+ AVs remained high (~90%) in both genotypes (Figure 2H), mirroring untreated conditions. By contrast, protease inhibition increased the fraction of aSyn+ AVs in the proximal axon to ~80% in both *PPM1H*$^{+/+}$ and *PPM1H*$^{-/-}$ neurons, eliminating the genotype-specific difference at untreated conditions (Figure 2I). Likewise, while the treatment had little effect on the density of aSyn-EGFP puncta in the distal axon, it abolished the genotype-dependent difference in the proximal axon (Figures 2J and 2K). Thus, lysosomal protease inhibition phenocopied the effects of PPM1H deficiency in WT neurons, supporting the conclusion that alterations in the proximal axon of untreated *PPM1H*$^{-/-}$ neurons reflect defective autophagosomal degradation.

Using the dual-color lysosomal reporter SEP-LAMP1-RFP, we found no difference in the acidification of axonal LAMP1 vesicles between *PPM1H*$^{+/+}$ and *PPM1H*$^{-/-}$ neurons (Figures S1J–S1K), arguing against a primary lysosomal defect underlying impaired aSyn degradation.

PFF-induced aSyn aggregation is aggravated in primary *PPM1H* KO neurons but not in human *PPM1H* KO or *LRRK2*-p.R1441H KI iNeurons

Previous work has shown that neurons expressing hyperactive LRRK2 exhibit exacerbated aSyn aggregate formation upon PFF treatment, with aggregates primarily located in axons.[28–31] We hypothesized that this phenotype is caused by RAB hyperphosphorylation, resulting in defective AV transport and maturation, and asked whether *PPM1H* KO phenocopies the effect of hyperactive LRRK2 on aSyn aggregation. We first assessed aSyn aggregation in iPSC-derived *PPM1H*$^{-/-}$ iNeurons, which show increased levels of LRRK2-phosphorylated RAB proteins.[13] iNeurons were exposed to PFFs on DIV14 and fixed 2 or 3 weeks later (DIV28 or DIV35) for phosphoserine 129 (pS129) immunolabeling of aSyn aggregates (Figure S2A). As expected, PFF, but not PBS, treatment induced aggregate formation (Figure S2B). For quantification of aSyn aggregation, pS129-positive area was normalized to MAP2 area as a proxy of neuronal density, as established in the published literature.[31,36–39]

Comparing PFF-induced aggregation between *PPM1H*$^{-/-}$ and WT iNeurons, we observed no difference in pS129-positive area at either DIV28 or DIV35 (Figures S2C–S2F). However, expression of hyperactive *LRRK2*-p.R1441H also did not result in a significant increase in pS129-positive aggregates at either time point (Figures S2C–S2F). Thus, under the conditions used, neither PPM1H loss nor hyperactive LRRK2

Figure 2. Knockout of PPM1H impairs the autophagosomal degradation of axonal aSyn-EGFP

(A) Schematic depicting physiological *en route* maturation of AVs during retrograde axonal transport.

(B) Kymographs of mScarlet-LC3 vesicles and aSyn-EGFP in the proximal axon of *PPM1H*$^{+/+}$ and *PPM1H*$^{-/-}$ mouse cortical neurons. Arrowheads: magenta, mScarlet-LC3-positive; green, aSyn-EGFP-positive; white, mScarlet-LC3- and aSyn-EGFP-positive.

(C–F) Fraction of AVs positive for aSyn-EGFP and number of aSyn-EGFP puncta normalized to 100 μm axonal length in the distal axon (C and E) (n = 11 neurons from three independent experiments; ns, not significant; $p > 0.3484$; mixed effects model analysis) and proximal axon (D and F) (n = 21–22 neurons from three independent experiments; $^{*}p = 0.0205$, $^{**}p = 0.0023$; mixed effects model analysis) of *PPM1H*$^{+/+}$ and *PPM1H*$^{-/-}$ neurons.

(G) Kymographs of mScarlet-LC3 vesicles and aSyn-EGFP in the proximal axon of *PPM1H*$^{+/+}$ and *PPM1H*$^{-/-}$ mouse cortical neurons treated with 10 μM E64d and 10 μM pepstatin A overnight.

(H–K) Fraction of AVs positive for aSyn-EGFP and number of aSyn-EGFP puncta in the distal axon (H and J) (n = 10–11 neurons from three independent experiments; ns, not significant; $p > 0.4258$; mixed effects model analysis) and proximal axon (I and K) (n = 15–16 neurons from three independent experiments; ns, not significant; $p > 0.4702$; mixed effects model analysis) of *PPM1H*$^{+/+}$ and *PPM1H*$^{-/-}$ neurons treated with protease inhibitors. Horizontal dashed lines in (I) and (K) indicate the respective average in untreated *PPM1H*$^{+/+}$ neurons. Scatterplot points indicate the means of three independent experiments, and error bars show mean ± SD of these points.

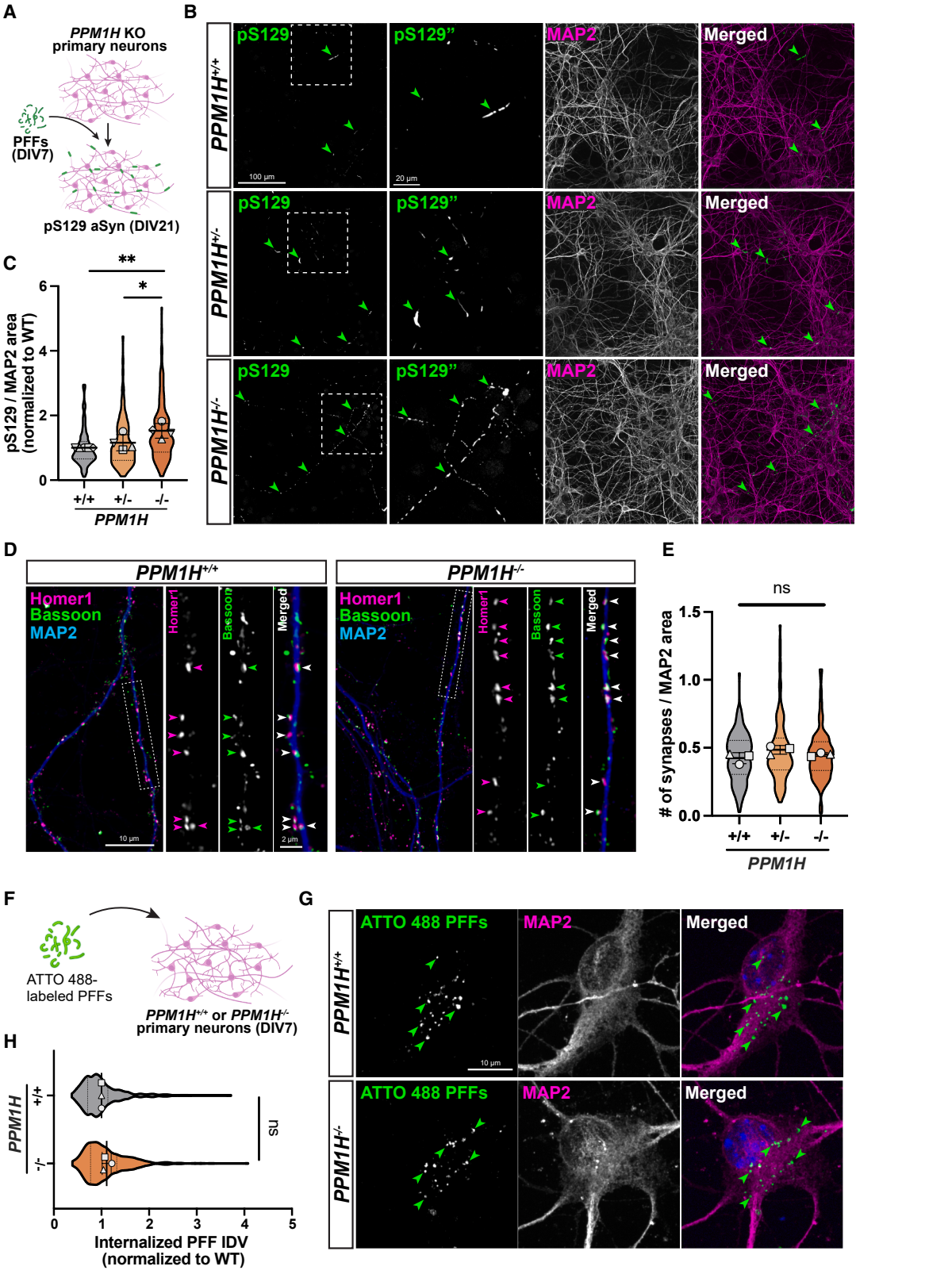

(legend on next page)

expression altered PFF-induced aggregation in iNeurons, suggesting that this model may lack sensitivity to detect such effects.

One possible explanation is that, similar to other iPSC-derived neurons, iNeurons exhibit slow synaptogenesis, resulting in a low density of synapses under conditions comparable to those in our study.[40] Consistent with this, we observed markedly fewer presynaptic puncta (synapsin puncta associated with MAP2-positive dendrites) in iNeurons at DIV28 as compared to primary mouse cortical neurons at DIV21 (Figures S3A and S3B). We also noted striking differences in the distribution of endogenous aSyn. While primary neurons displayed strong enrichment of aSyn at presynaptic puncta, iNeurons showed a more diffuse axonal aSyn signal, with only sparse presynaptic enrichment (Figure S3A). This pattern resembles that reported in immature (DIV6) primary neurons, where aSyn is largely cytosolic with limited synaptic presence.[41]

Given prior reports that aSyn aggregation is dependent on synaptic activity,[32] we hypothesized that the more synaptically mature primary neurons might provide a more sensitive system to detect effects of RAB hyperphosphorylation on aSyn aggregation. Littermate-derived *PPM1H*$^{+/+}$, *PPM1H*$^{+/-}$, and *PPM1H*$^{-/-}$ mouse cortical neurons were exposed to PFFs on DIV7 and fixed for pS129 immunostaining on DIV21 (Figure 3A). PFF, but not PBS or aSyn monomer, treatment induced robust pS129-positive aggregation (Figures S3C–S3E).

Strikingly, *PPM1H*$^{-/-}$ neurons showed a significant increase in pS129-positive area compared to *PPM1H*$^{+/+}$ controls (Figures 3B and 3C), while *PPM1H*$^{+/-}$ neurons exhibited a non-significant upward trend (Figures 3B and 3C). Further analysis revealed that *PPM1H*$^{-/-}$ neurons contained both larger and more frequent aggregates, indicating that the increase in overall pS129-positive area reflects an increase in both aggregate size and frequency (Figures S3F and S3G). MAP2 area was unchanged across genotypes (Figure S3H), excluding a confounding effect of neuronal loss.

We noted that most aggregates localized outside of the MAP2-positive compartment (Figure S3D), likely representing axonal localization as previously described.[28–31] Only a small number of somata contained detectable aggregates, precluding meaningful quantification of their frequency in randomly imaged fields. Instead, we screened coverslips for somata with aggregates and compared aggregate area, finding no significant effect of PPM1H loss (Figures S4A and S4B).

Together, our data show that primary *PPM1H*$^{-/-}$ neurons phenocopy the aggravated aSyn aggregation previously reported in neurons expressing hyperactive LRRK2.[28–31] The predominant localization of aggregates outside of the MAP2-positive compartment and absence of a detectable effect on somatic aggregate size support the idea that the enhanced aggregation is driven by axonal pathology.

Enhanced aSyn aggregation in primary *PPM1H* KO neurons is not caused by altered protein expression, synaptic density, or somatic PFF uptake

Since altered aSyn or LRRK2 expression could confound aggregation phenotypes,[42] we assessed their levels in *PPM1H*$^{+/+}$, *PPM1H*$^{+/-}$, and *PPM1H*$^{-/-}$ primary neurons. Loss of PPM1H had no effect on intracellular aSyn levels at either DIV8 (Figures S1A and S1C) or DIV21 (Figures S4C and S4D) nor did it alter LRRK2 expression (Figures S4C–S4F). In contrast to the marked effect on pT73 RAB10, loss of PPM1H did not affect pS106 RAB12 phosphorylation (Figures S4C and S4G). This observation is consistent with prior reports demonstrating that PPM1H efficiently dephosphorylates RAB10 but has only minimal activity toward RAB12.[9,11]

Because aSyn aggregation can be influenced by synaptic connectivity,[32] we next assessed synaptic density. Synaptically mature DIV21 neurons were stained for the presynaptic marker bassoon and the postsynaptic marker homer1, and synapses were identified by the apposition of these markers. Quantification revealed no differences in synapse number between *PPM1H*$^{+/+}$, *PPM1H*$^{+/-}$, and *PPM1H*$^{-/-}$ primary neurons (Figures 3D and 3E), excluding altered synaptic density as a contributing factor.

We also tested whether PPM1H deficiency affects intracellular PFF uptake. *PPM1H*$^{+/+}$ and *PPM1H*$^{-/-}$ primary neurons were treated with ATTO-488-labeled PFFs, and internalized signal was quantified following removal of extracellular PFFs with diluted trypsin.[43] We observed no differences in the integrated density or area of internalized PFFs in the soma between genotypes (Figures 3F–3H; Figure S4H). We were not able to measure PFF uptake specifically into the axonal compartment, as axons proved highly sensitive to the trypsin wash required to eliminate extracellular PFFs. Taken together, these results indicate that

Figure 3. Knockout of PPM1H exacerbates PFF-induced aSyn aggregation in primary neurons

(A) Schematic depicting the experimental timeline.

(B) Representative images of DIV21 *PPM1H*$^{+/+}$, *PPM1H*$^{+/-}$, and *PPM1H*$^{-/-}$ neurons stained for pS129-positive aSyn aggregates and MAP2 upon PFF treatment on DIV7. Green arrowheads: pS129-positive aSyn aggregates. Dashed boxes are shown at higher magnification in the second column.

(C) pS129/MAP2 area in *PPM1H*$^{+/+}$, *PPM1H*$^{+/-}$, and *PPM1H*$^{-/-}$ neurons (n = 95–148 fields of view from five independent experiments; *$p < 0.0417$, **$p = 0.0029$; mixed effects model analysis).

(D) Representative images of DIV21 *PPM1H*$^{+/+}$ and *PPM1H*$^{-/-}$ mouse cortical neurons stained for the postsynaptic marker homer1 (magenta), the presynaptic marker bassoon (green), and the somatodendritic marker MAP2 (blue). Arrowheads highlight examples of synapses.

(E) Synapses per μm^2 of MAP2 area in *PPM1H*$^{+/+}$, *PPM1H*$^{+/-}$, and *PPM1H*$^{-/-}$ neurons (mean ± SD; n = 111–114 fields of view from three independent experiments; ns, not significant; $p > 0.2433$; mixed effects model analysis).

(F) Schematic depicting the experimental setup.

(G) Representative images of DIV8 *PPM1H*$^{+/+}$ and *PPM1H*$^{-/-}$ mouse cortical neurons exposed to ATTO 488-labeled PFFs for 24 h and stained for MAP2. Green arrowheads highlight examples of internalized PFFs.

(H) Integrated density of internalized ATTO-488-labeled PFFs normalized to WT control in *PPM1H*$^{+/+}$ and *PPM1H*$^{-/-}$ neurons (n = 270–301 neurons from three independent experiments; ns, not significant; $p = 0.1771$; mixed effects model analysis). Scatterplot points indicate the means of independent experiments, and error bars show mean ± SD of these points.

the enhanced aSyn aggregation in *PPM1H*$^{-/-}$ neurons is not due to altered aSyn or LRRK2 expression, increased synapse density, or enhanced somatic PFF uptake.

Early pS129-positive aggregates associate with autophagosome markers

To further investigate the link between aSyn aggregation and autophagy, we co-stained PFF-treated primary neurons for pS129-positive aggregates and autophagosome markers (Figure 4A). Given the limited size of autophagosomes, we reasoned that autophagy may preferentially target early aggregation intermediates rather than large, mature inclusions. We therefore analyzed neurons at an earlier time point (DIV14; 7 days after PFF treatment), when smaller aggregates are more abundant. We observed robust colocalization of small, rounded pS129-positive aggregates with the autophagosome markers LC3 and GABARAP family proteins (GABARAP/L1/L2), whereas larger, elongated aggregates showed no clear colocalization with either marker (Figure 4B). These findings demonstrate that early aSyn aggregates are associated with autophagosome markers and, together with the autophagy defects described above, support a model in which dysfunctional axonal autophagy in *PPM1H* KO neurons impairs efficient clearance, thereby leading to enhanced aggregate accumulation.

Exacerbated PFF-induced aSyn aggregation in primary *PPM1H* KO neurons is dependent on LRRK2 kinase activity

To determine whether the increased aggregation in PPM1H-deficient neurons is mediated through a LRRK2-dependent pathway, we treated primary *PPM1H* KO neurons with the selective LRRK2 kinase inhibitor MLi-2. Neurons were treated with MLi-2 or DMSO control on DIV5, exposed to PFFs on DIV7, and fixed and stained for pS129 aggregates on DIV21 (Figure 4C). Western blot analysis confirmed that MLi-2 reduced pT73 RAB10 phosphorylation in *PPM1H*$^{-/-}$ neurons to levels comparable to those in *PPM1H*$^{+/+}$ controls (Figure 4D). Quantification of pS129-positive area revealed that LRRK2 inhibition reduced aSyn aggregation in *PPM1H*$^{-/-}$ neurons to *PPM1H*$^{+/+}$ control levels (Figures 4E and 4F). In contrast, MLi-2 did not alter aggregate burden in *PPM1H*$^{+/+}$ neurons (Figures 4E and 4F). These results demonstrate that the increased aSyn aggregation observed in *PPM1H*$^{-/-}$ neurons is dependent on LRRK2 kinase activity.

DISCUSSION

Here, we identify the LRRK2-counteracting RAB phosphatase PPM1H as an important regulator of axonal autophagy and aSyn proteostasis in neurons. We show that loss of PPM1H disrupts axonal AV transport, impairs the autophagosomal degradation of overexpressed aSyn, and exacerbates aSyn aggregate formation upon exposure to PFFs in a LRRK2-kinase-dependent manner. These findings provide evidence that RAB hyperphosphorylation mechanistically links elevated LRRK2 activity to defective axonal autophagy and enhanced aSyn pathology.

We found that axonal AV transport was markedly impaired in primary *PPM1H* KO neurons. Treatment with the selective LRRK2 inhibitor MLi-2 rescued this defect to levels comparable to those in untreated *PPM1H*$^{+/+}$ neurons, confirming that the disruption of AV transport induced by loss of PPM1H is dependent on LRRK2 kinase activity. Interestingly, *PPM1H*$^{-/-}$ neurons showed a more pronounced disruption of AV transport than *PPM1H*$^{+/-}$ neurons, revealing a gene dosage effect in which transport deficits scale with the level of RAB hyperphosphorylation. This model is consistent with prior observations that the strongly hyperactivating *LRRK2*-p.R1441H mutation disrupts AV transport to a greater extent than the moderately hyperactivating *LRRK2*-p.G2019S mutation.[13] Notably, the more severe transport disruption in *PPM1H*$^{-/-}$ neurons correlated with greater aSyn aggregation than in *PPM1H*$^{+/-}$ neurons.

Several previous studies have demonstrated that impairment of retrograde AV transport—via diverse mechanisms—leads to defective AV maturation, disrupting effective axonal degradation of autophagosomal cargo.[12,21,23] To investigate whether impaired AV transport affects the autophagosomal degradation of aSyn, we challenged *PPM1H* KO neurons with aSyn overexpression. We found that defective AV transport in *PPM1H*$^{-/-}$ primary neurons was accompanied by both an increased fraction of AVs containing aSyn-EGFP and an increased density of aSyn-EGFP puncta in the proximal axon, while we observed no difference between genotypes in the distal axon. These findings were recapitulated in *PPM1H*$^{-/-}$ iNeurons, which similarly showed an increased fraction of aSyn+ AVs in the proximal axon. Notably, treatment with lysosomal protease inhibitors eliminated genotype-specific differences in the proximal axon, supporting the idea that these effects reflect impaired autophagosomal degradation. Mechanistically, our finding that loss of PPM1H did not affect the acidification of axonal LAMP1 vesicles argues against a primary lysosomal defect underlying impaired aSyn degradation. We instead propose that defective retrograde transport of AVs reduces fusion with lysosomes—an event that is already infrequent in axons—[19]thereby leading to impaired cargo degradation.

Expression of hyperactive LRRK2 has been shown to exacerbate accumulation of aSyn aggregates upon PFF treatment in a number of previous studies.[28–31] We found that primary *PPM1H* KO neurons phenocopied this effect, showing significantly increased aSyn aggregation upon PFF treatment. Both the number and size of individual aggregates were increased in *PPM1H*$^{-/-}$ neurons, resulting in an overall ~1.5-fold higher pS129-positive area compared to littermate *PPM1H*$^{+/+}$ controls. Heterozygous *PPM1H*$^{+/-}$ neurons showed a similar upward trend in aggregate area. Importantly, pharmacological LRRK2 kinase inhibition with MLi-2 rescued aSyn aggregation in *PPM1H*$^{-/-}$ neurons to WT levels, strongly supporting that the exacerbated aggregation in this genotype is mediated by LRRK2-mediated RAB hyperphosphorylation. In contrast, MLi-2 had no detectable effect in *PPM1H*$^{+/+}$ neurons, indicating that reducing LRRK2 kinase activity does not further ameliorate aSyn aggregation when RAB phosphorylation is already at WT levels. While this differs from some earlier reports of reduced aSyn aggregation upon LRRK2 inhibition in WT neurons,[28,44] it aligns with more recent PFF- or AAV-based studies showing no effect in LRRK2-WT backgrounds.[45,46]

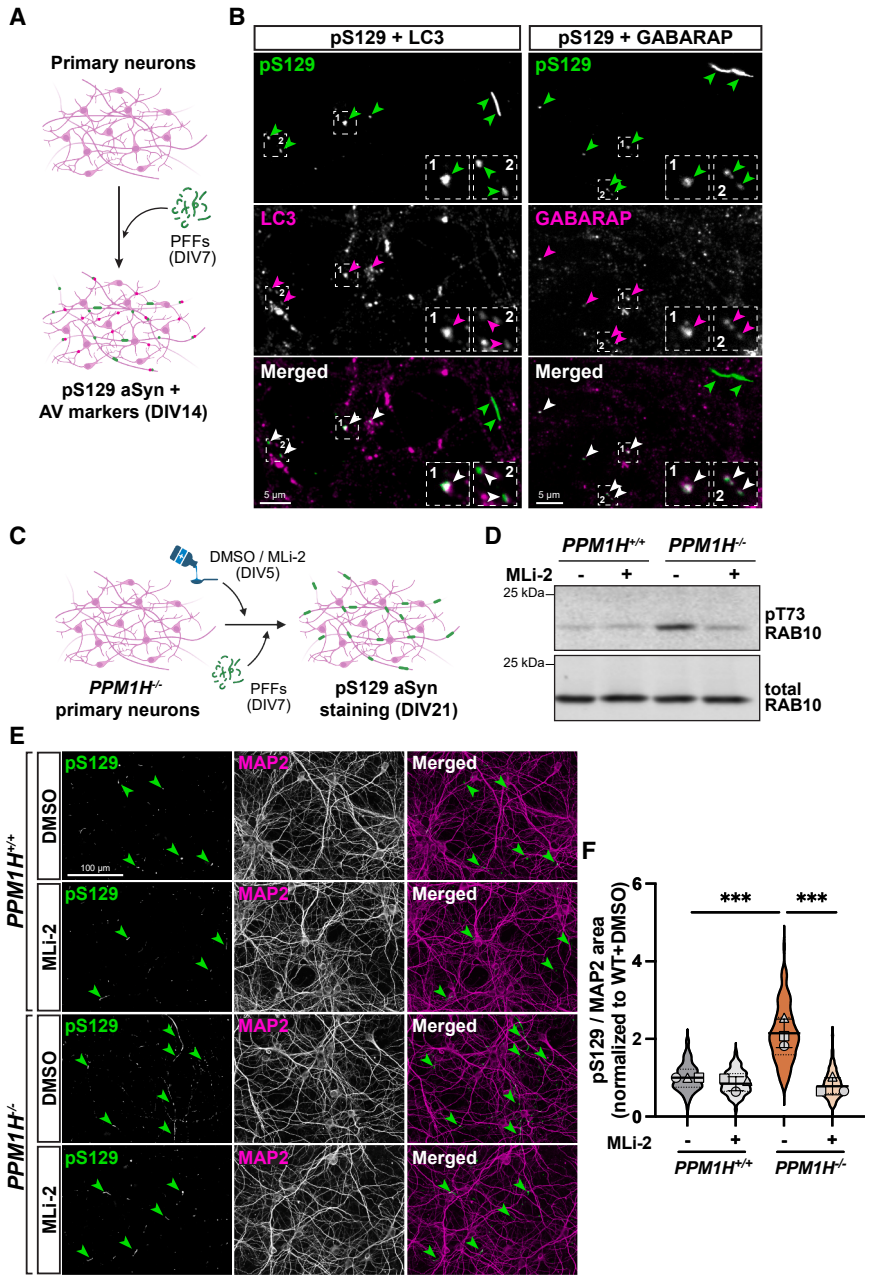

Figure 4. LRRK2 kinase inhibition rescues PFF-induced aSyn aggregation in primary PPM1H knockout neurons

(A) Schematic depicting the experimental setup.

(B) Representative images of DIV14 primary cortical neurons stained for pS129-positive aSyn aggregates and LC3 or GABARAP family proteins after 7 days of incubation with PFFs. Arrowheads: green, pS129-positive, magenta, LC3- or GABARAP-positive; white, LC3-/GABARAP- and pS129-positive.

(C) Schematic depicting the experimental timeline.

(D) Western blot of pT73 RAB10 and total RAB10 in DIV21 *PPM1H*$^{+/+}$ and *PPM1H*$^{-/-}$ mouse cortical neurons treated with DMSO or 300 nM MLi-2 until cell lysis on DIV21.

(E) Representative images of DIV21 *PPM1H*$^{+/+}$ and *PPM1H*$^{-/-}$ neurons treated with DMSO or MLi-2 and stained for pS129-positive aSyn aggregates and MAP2 after 14 days of incubation with PFFs. Green arrowheads highlight examples of pS129-positive aSyn aggregates.

(F) pS129/MAP2 area normalized to DMSO control in *PPM1H*$^{+/+}$ and *PPM1H*$^{-/-}$ neurons treated with DMSO or MLi-2 (mean ± SD; n = 77–99 fields of view from three independent experiments; ***$p < 0.001$; mixed effects model analysis). Scatterplot points indicate the means of three independent experiments.

To identify possible confounding factors that may influence aSyn aggregation, we assessed aSyn and LRRK2 expression, synaptic density, as well as intracellular PFF uptake across *PPM1H* KO genotypes. Enhanced aggregation in *PPM1H*$^{-/-}$ neurons was not attributable to altered protein levels, synapse number, or somatic uptake of PFFs, consistent with a previous report showing no effect of hyperactive LRRK2 on neuronal PFF internalization.[30] Instead, the co-localization of early pS129-positive aggregates with autophagosome markers supports a model in which defective AV transport and impaired axonal aSyn degradation result in increased neuronal vulnerability to PFF-induced aSyn aggregation. An intriguing possibility is that exacerbated aggregation reflects not only impaired degradation but also compensatory activation of secretory autophagy, which has recently been reported in neurons with LRRK2-mediated defects in axonal autophagy.[47] Such a pathway could facilitate cell-to-cell spread of pathogenic aSyn species, a mechanistic link that warrants direct investigation in future studies.

Interestingly, neither the loss of PPM1H nor the expression of hyperactive LRRK2 had a detectable impact on aSyn aggregation in iPSC-derived iNeurons, in contrast to the robust effect in primary *PPM1H*$^{-/-}$ neurons. Given prior reports that the detrimental effect of hyperactive LRRK2 on aSyn aggregation is dependent on synaptic activity,[32] we compared synaptic maturity between the two models. We observed striking differences: while primary neurons displayed abundant synapses and strong enrichment of endogenous aSyn at presynapses, iNeurons exhibited fewer synapses and a more diffuse intraaxonal distribution of aSyn. Mechanistically, the strong enrichment of aSyn at the presynapse, a major site of autophagosome biogenesis, may increase reliance on axonal autophagy for aSyn clearance in primary neurons, making them more vulnerable to defects in this pathway. Together, our findings suggest that differences in synaptic maturity and aSyn compartmentalization determine whether defects in AV transport and degradation translate into detectable changes of endogenous aSyn aggregation.

A puzzling but interesting finding of neuropathological studies is that despite being clinically almost indistinguishable from idiopathic PD, about 20%–50% of cases with LRRK2-PD do not show the hallmark pathology of aSyn aggregation into Lewy bodies and Lewy neurites.[48] Two recent studies help resolve this discrepancy, showing that aSyn oligomers, representing an earlier stage of aSyn aggregation, are consistently present even in Lewy-negative LRRK2-PD brains.[49,50] Our data are compatible with a model in which impaired axonal degradation promotes accumulation of early aggregation species, whereas progression to mature Lewy pathology may depend on the complex multicellular environment of the brain and/or additional cellular or environmental "second hits." Directly assessing aSyn oligomers in the mouse neurons primarily used in our study is currently hampered by the lack of a reliable proximity ligation assay to detect mouse oligomers,[51] an important goal for future studies.

In summary, our study shows that loss of the LRRK2-counteracting RAB phosphatase PPM1H disrupts the axonal transport of autophagosomes, impairs the autophagosomal degradation of axonal aSyn, and exacerbates the PFF-induced aggregation of aSyn in an LRRK2-kinase-dependent manner. The finding that PPM1H deficiency phenocopies the effects of hyperactive LRRK2 on autophagy and aSyn pathology provides compelling mechanistic support for the LRRK2-RAB axis as a driver of PD pathology. Clarifying how LRRK2 hyperactivity leads to neurodegeneration has important translational implications, particularly as reported side effects of LRRK2 kinase inhibitors may necessitate more selective therapeutic strategies.

Limitations of the study

Our work mechanistically links the LRRK2-pRAB-PPM1H axis to defects in axonal autophagy and exacerbated aSyn aggregation; however, the specific pRAB mediating this phenotype remains to be identified. Based on current evidence, pRAB10 appears most plausible, as it is efficiently dephosphorylated by PPM1H and has been implicated in recruitment of JIP4—the motor adaptor protein mediating the "tug-of-war" underlying defective AV transport—to organelles.[9,52,53] In addition, a role for RAB10 in regulating AV transport is supported by data from wild-type neurons,[54] and proteomic and western blot analyses indicate that LRRK2, RAB10, and PPM1H all associate with the outer AV membrane.[12,55] The absence of elevated pRAB12 levels in *PPM1H* KO neurons argues against a major role for this RAB. While PPM1H emerges as a key regulator of axonal autophagy and aSyn aggregation, potential contributions of additional phosphatases, such as PPM1M,[11] cannot be excluded. Moreover, although we did not detect alterations in lysosomal acidification, more subtle or context-dependent alterations in lysosome function may still contribute to the observed phenotype. Finally, it remains to be determined how the cellular mechanisms described here contribute to disease pathogenesis *in vivo* in patients with PD.

RESOURCE AVAILABILITY

Lead contact

Further information and requests for resources and reagents should be directed to and will be fulfilled by the lead contact, C. Alexander Boecker (alexander.boecker@med.uni-goettingen.de).

Materials availability

Unique reagents generated in this study are available from the lead contact with a completed Materials Transfer Agreement.

Data and code availability

- All data reported in this paper will be shared by the lead contact upon request.
- This paper does not report original code.
- Any additional information required to reanalyze the data reported in this paper is available from the lead contact upon request.

ACKNOWLEDGMENTS

We thank the Live-Cell Imaging Facility of the Max Planck Institute for Multidisciplinary Sciences, Goettingen, Germany for providing access to the Visitron CSU-W1 Spinning Disk confocal system and especially Peter Lenart and Antonio Z. Politi for technical support. We thank the Light Microscopy Facility of the European Neuroscience Institute Goettingen for providing access to the Zeiss LSM800 laser scanning confocal system and Lisbeth Harder for technical support, as well as Dan Dou, University of Pennsylvania, for helpful insights and discussions. Cartoon schematics were created in part with BioRender.com. The authors gratefully acknowledge support from the

Michael J. Fox Foundation (MJFF-021130 to C.A.B. and E.L.F.H.), the NIH (R01 NS060698 to E.L.F.H.), and the Else Kröner-Fresenius-Stiftung (2023_EKEA.91 to C.A.B.). M.F. and A.M. were supported by intramural fellowships of the University Medical Center Goettingen. T.F.O. is supported by DFG SFB1286 (B8).

AUTHOR CONTRIBUTIONS

Conceptualization, M.F., A.M., and C.A.B.; methodology M.F., A.M., L.E., M.-S.C.O., M.A.-A., T.F.O., and M.Z.; investigation M.F., A.M., L.E., B.T., J.M.G., M.-S.C.O., M.A.-A., and C.A.B.; writing – original draft, M.F., A.M., and C.A.B.; writing – review and editing, M.F., A.M., L.E., B.T., J.M.G., M.-S.C.O., M.A.-A., T.F., M.Z., E.L.F.H., and C.A.B.; funding acquisition, E.L.F.H. and C.A.B.; supervision, E.L.F.H. and C.A.B.

DECLARATION OF INTERESTS

The authors declare no competing interests.

STAR★METHODS

Detailed methods are provided in the online version of this paper and include the following:

- KEY RESOURCES TABLE
- EXPERIMENTAL MODEL AND STUDY PARTICIPANT DETAILS
  - Primary neuron culture
  - PiggyBac-mediated iPSC-derived neuron differentiation and iNeuron culture
- METHOD DETAILS
  - Live-cell imaging
  - PFF assay
  - ATTO 488-labeled PFF assay
  - Immunofluorescence
  - Immunoblotting
- QUANTIFICATION AND STATISTICAL ANALYSIS
  - AV motility
  - Fraction of aSyn-EGFP-positive AVs and number of aSyn-EGFP puncta
  - Lysosome acidification
  - PFF assay
  - Presynapse and synapse number
  - Tagged PFF assay
  - Statistical analysis

SUPPLEMENTAL INFORMATION

Supplemental information can be found online at https://doi.org/10.1016/j.celrep.2026.117364.

Received: September 26, 2025
Revised: March 12, 2026
Accepted: April 17, 2026
Published: May 21, 2026

REFERENCES

1. Steger, M., Tonelli, F., Ito, G., Davies, P., Trost, M., Vetter, M., Wachter, S., Lorentzen, E., Duddy, G., Wilson, S., et al. (2016). Phosphoproteomics reveals that Parkinson's disease kinase LRRK2 regulates a subset of Rab GTPases. eLife *5*, e12813. https://doi.org/10.7554/eLife.12813.
2. Steger, M., Diez, F., Dhekne, H.S., Lis, P., Nirujogi, R.S., Karayel, O., Tonelli, F., Martinez, T.N., Lorentzen, E., Pfeffer, S.R., et al. (2017). Systematic proteomic analysis of LRRK2-mediated rab GTPase phosphorylation establishes a connection to ciliogenesis. eLife *6*, e31012. https://doi.org/10.7554/eLife.31012.
3. Mir, R., Tonelli, F., Lis, P., Macartney, T., Polinski, N.K., Martinez, T.N., Chou, M.-Y., Howden, A.J.M., König, T., Hotzy, C., et al. (2018). The Parkinson's disease VPS35[D620N] mutation enhances LRRK2-mediated Rab protein phosphorylation in mouse and human. Biochem. J. *475*, 1861–1883. https://doi.org/10.1042/BCJ20180248.
4. Gustavsson, E.K., Follett, J., Trinh, J., Barodia, S.K., Real, R., Liu, Z., Grant-Peters, M., Fox, J.D., Appel-Cresswell, S., Stoessl, A.J., et al. (2024). *RAB32* Ser71Arg in autosomal dominant Parkinson's disease: linkage, association, and functional analyses. Lancet Neurol. *23*, 603–614. https://doi.org/10.1016/S1474-4422(24)00121-2.
5. Hop, P.J., Lai, D., Keagle, P.J., Baron, D.M., Kenna, B.J., Kooyman, M., Asselta, R., , et al.Halter, C., Halter, C., Straniero, L. (2024). Systematic rare variant analyses identify RAB32 as a susceptibility gene for familial Parkinson's disease. Nat. Genet. *56*, 1371–1376. https://doi.org/10.1038/s41588-024-01787-7.
6. De Miranda, B.R., Castro, S.L., Rocha, E.M., Bodle, C.R., Johnson, K.E., and Greenamyre, J.T. (2021). The industrial solvent trichloroethylene induces LRRK2 kinase activity and dopaminergic neurodegeneration in a rat model of Parkinson's disease. Neurobiol. Dis. *153*, 105312. https://doi.org/10.1016/j.nbd.2021.105312.
7. Ilieva, N.M., Hoffman, E.K., Ghalib, M.A., Greenamyre, J.T., and De Miranda, B.R. (2024). LRRK2 kinase inhibition protects against Parkinson's disease-associated environmental toxicants. Neurobiol. Dis. *196*, 106522. https://doi.org/10.1016/j.nbd.2024.106522.
8. Di Maio, R., Hoffman, E.K., Rocha, E.M., Keeney, M.T., Sanders, L.H., De Miranda, B.R., Zharikov, A., Van Laar, A., Stepan, A.F., Lanz, T.A., et al. (2018). LRRK2 activation in idiopathic Parkinson's disease. Sci. Transl. Med. *10*, eaar5429. https://doi.org/10.1126/scitranslmed.aar5429.
9. Berndsen, K., Lis, P., Yeshaw, W.M., Wawro, P.S., Nirujogi, R.S., Wightman, M., Macartney, T., Dorward, M., Knebel, A., Tonelli, F., et al. (2019). PPM1H phosphatase counteracts LRRK2 signaling by selectively dephosphorylating Rab proteins. eLife *8*, e50416. https://doi.org/10.7554/eLife.50416.
10. Khan, S.S., Jaimon, E., Lin, Y.-E., Nikoloff, J., Tonelli, F., Alessi, D.R., and Pfeffer, S.R. (2024). Loss of primary cilia and dopaminergic neuroprotection in pathogenic LRRK2-driven and idiopathic Parkinson's disease. Proc. Natl. Acad. Sci. *121*, e2402206121. https://doi.org/10.1101/2024.01.15.575737.
11. Chiang, C.Y., Pratuseviciute, N., Lin, Y.-E., Adhikari, A., Yeshaw, W.M., Flitton, C., Sherpa, P.L., Tonelli, F., Rektorova, I., Lynch, T., et al. (2025). PPM1M, an LRRK2-counteracting, phosphoRab12-preferring phosphatase with a potential link to Parkinson's disease. Cell Rep. *44*, 116031. https://doi.org/10.1016/j.celrep.2025.116031.
12. Boecker, C.A., Goldsmith, J., Dou, D., Cajka, G.G., and Holzbaur, E.L.F. (2021). Increased LRRK2 kinase activity alters neuronal autophagy by disrupting the axonal transport of autophagosomes. Curr. Biol. *31*, 2140–2154.e6. https://doi.org/10.1016/j.cub.2021.02.061.
13. Dou, D., Smith, E.M., Evans, C.S., Boecker, C.A., and Holzbaur, E.L.F. (2023). Regulatory imbalance between LRRK2 kinase, PPM1H phosphatase, and ARF6 GTPase disrupts the axonal transport of autophagosomes. Cell Rep. *42*, 112448. https://doi.org/10.1016/j.celrep.2023.112448.
14. Twellsieck, B., and Boecker, C.A. (2025). Role of LRRK2 in axonal transport and Parkinson's disease. Biochem. J. *482*, 905–919. https://doi.org/10.1042/BCJ20253133.
15. Maday, S., Wallace, K.E., and Holzbaur, E.L.F. (2012). Autophagosomes initiate distally and mature during transport toward the cell soma in primary neurons. J. Cell Biol. *196*, 407–417. https://doi.org/10.1083/jcb.201106120.
16. Maday, S., and Holzbaur, E.L.F. (2014). Autophagosome biogenesis in primary neurons follows an ordered and spatially regulated pathway. Dev. Cell *30*, 71–85. https://doi.org/10.1016/j.devcel.2014.06.001.
17. Neisch, A.L., Neufeld, T.P., and Hays, T.S. (2017). A STRIPAK complex mediates axonal transport of autophagosomes and dense core vesicles

through PP2A regulation. J. Cell Biol. *216*, 441–461. https://doi.org/10.1083/jcb.201606082.

18. Stavoe, A.K.H., Kargbo-Hill, S.E., Hall, D.H., and Colón-Ramos, D.A. (2016). KIF1A/UNC-104 Transports ATG-9 to Regulate Neurodevelopment and Autophagy at Synapses. Dev. Cell *38*, 171–185. https://doi.org/10.1016/j.devcel.2016.06.012.
19. Cason, S.E., Mogre, S.S., Holzbaur, E.L.F., and Koslover, E.F. (2022). Spatiotemporal analysis of axonal autophagosome-lysosome dynamics reveals limited fusion events and slow maturation. Mol. Biol. Cell *33*, ar123. https://doi.org/10.1091/mbc.E22-03-0111.
20. Farfel-Becker, T., Roney, J.C., Cheng, X.T., Li, S., Cuddy, S.R., and Sheng, Z.H. (2019). Neuronal Soma-Derived Degradative Lysosomes Are Continuously Delivered to Distal Axons to Maintain Local Degradation Capacity. Cell Rep. *28*, 51–64.e4. https://doi.org/10.1016/j.celrep.2019.06.013.
21. Wong, Y.C., and Holzbaur, E.L.F. (2014). The Regulation of Autophagosome Dynamics by Huntingtin and HAP1 Is Disrupted by Expression of Mutant Huntingtin, Leading to Defective Cargo Degradation. J. Neurosci. *34*, 1293–1305. https://doi.org/10.1523/JNEUROSCI.1870-13.2014.
22. Cason, S.E., Carman, P.J., Van Duyne, C., Goldsmith, J., Dominguez, R., and Holzbaur, E.L.F. (2021). Sequential dynein effectors regulate axonal autophagosome motility in a maturation-dependent pathway. J. Cell Biol. *220*, e202010179. https://doi.org/10.1083/jcb.202010179.
23. Fu, M.M., Nirschl, J.J., and Holzbaur, E.L.F. (2014). LC3 Binding to the Scaffolding Protein JIP1 Regulates Processive Dynein-Driven Transport of Autophagosomes. Dev. Cell *29*, 577–590. https://doi.org/10.1016/j.devcel.2014.04.015.
24. Goldsmith, J., Ordureau, A., Ca, C.A.B., Arany, M., Harper, J.W., and Holzbaur, E.L. (2023). Proteomics analysis of autophagy cargos reveals distinct adaptations in PINK1 and LRRK2 models of Parkinson disease. Preprint at bioRxiv. https://doi.org/10.1101/2022.10.03.510717.
25. Friedman, L.G., Lachenmayer, M.L., Wang, J., He, L., Poulose, S.M., Komatsu, M., Holstein, G.R., and Yue, Z. (2012). Disrupted Autophagy Leads to Dopaminergic Axon and Dendrite Degeneration and Promotes Presynaptic Accumulation of -Synuclein and LRRK2 in the Brain. J. Neurosci. *32*, 7585–7593. https://doi.org/10.1523/JNEUROSCI.5809-11.2012.
26. Vogiatzi, T., Xilouri, M., Vekrellis, K., and Stefanis, L. (2008). Wild type α-synuclein is degraded by chaperone-mediated autophagy and macroautophagy in neuronal cells. J. Biol. Chem. *283*, 23542–23556. https://doi.org/10.1074/jbc.M801992200.
27. Braak, H., Del Tredici, K., Rüb, U., De Vos, R.A.I., Jansen Steur, E.N.H., and Braak, E. (2003). Staging of brain pathology related to sporadic Parkinson's disease. Neurobiol. Aging *24*, 197–211. https://doi.org/10.1016/S0197-4580(02)00065-9.
28. Volpicelli-Daley, L.A., Abdelmotilib, H., Liu, Z., Stoyka, L., Daher, J.P.L., Milnerwood, A.J., Unni, V.K., Hirst, W.D., Yue, Z., Zhao, H.T., et al. (2016). G2019S-LRRK2 expression augments α-synuclein sequestration into inclusions in neurons. J. Neurosci. *36*, 7415–7427. https://doi.org/10.1523/JNEUROSCI.3642-15.2016.
29. MacIsaac, S., Quevedo Melo, T., Zhang, Y., Volta, M., Farrer, M.J., and Milnerwood, A.J. (2020). Neuron-autonomous susceptibility to induced synuclein aggregation is exacerbated by endogenous Lrrk2 mutations and ameliorated by Lrrk2 genetic knock-out. Brain Commun. *2*, fcz052. https://doi.org/10.1093/braincomms/fcz052.
30. Bieri, G., Brahic, M., Bousset, L., Couthouis, J., Kramer, N.J., Ma, R., Nakayama, L., Monbureau, M., Defensor, E., Schüle, B., et al. (2019). LRRK2 modifies α-syn pathology and spread in mouse models and human neurons. Acta Neuropathol. *137*, 961–980. https://doi.org/10.1007/s00401-019-01995-0.
31. Henderson, M.X., Peng, C., Trojanowski, J.Q., and Lee, V.M.Y. (2018). LRRK2 activity does not dramatically alter α-synuclein pathology in primary neurons. Acta Neuropathol. Commun. *6*, 45. https://doi.org/10.1186/s40478-018-0550-0.
32. Wu, Q., Shaikh, M.A., Meymand, E.S., Zhang, B., Luk, K.C., Trojanowski, J.Q., and Lee, V.M.-Y. (2020). Neuronal activity modulates alpha-synuclein aggregation and spreading in organotypic brain slice cultures and in vivo. Acta Neuropathol. *140*, 831–849. https://doi.org/10.1007/s00401-020-02227-6.
33. Khan, S.S., Sobu, Y., Dhekne, H.S., Tonelli, F., Berndsen, K., Alessi, D.R., and Pfeffer, S.R. (2021). Pathogenic LRRK2 control of primary cilia and Hedgehog signaling in neurons and astrocytes of mouse brain. eLife *10*, e67900. https://doi.org/10.7554/eLife.67900.
34. Fell, M.J., Mirescu, C., Basu, K., Cheewatrakoolpong, B., DeMong, D.E., Ellis, J.M., Hyde, L.A., Lin, Y., Markgraf, C.G., Mei, H., et al. (2015). MLi-2, a Potent, Selective, and Centrally Active Compound for Exploring the Therapeutic Potential and Safety of LRRK2 Kinase Inhibition. J. Pharmacol. Exp. Ther. *355*, 397–409. https://doi.org/10.1124/jpet.115.227587.
35. Tanida, I., Minematsu-Ikeguchi, N., Ueno, T., and Kominami, E. (2005). Lysosomal Turnover, but Not a Cellular Level, of Endogenous LC3 is a Marker for Autophagy. Autophagy *1*, 84–91. https://doi.org/10.4161/auto.1.2.1697.
36. Henderson, M.X., Sedor, S., McGeary, I., Cornblath, E.J., Peng, C., Riddle, D.M., Li, H.L., Zhang, B., Brown, H.J., Olufemi, M.F., et al. (2020). Glucocerebrosidase Activity Modulates Neuronal Susceptibility to Pathological α-Synuclein Insult. Neuron *105*, 822–836.e7. https://doi.org/10.1016/j.neuron.2019.12.004.
37. Emmenegger, M., De Cecco, E., Hruska-Plochan, M., Eninger, T., Schneider, M.M., Barth, M., Tantardini, E., de Rossi, P., Bacioglu, M., Langston, R.G., et al. (2021). LAG3 is not expressed in human and murine neurons and does not modulate α-synucleinopathies. EMBO Mol. Med. *13*, e14745. https://doi.org/10.15252/emmm.202114745.
38. Yu, T., Nie, S., Bu, L., Liu, M., He, J., Niu, X., Feng, H., Guo, J., Tang, B., Zhang, Z., et al. (2023). Cholestanol accelerates α-synuclein aggregation and spreading by activating asparagine endopeptidase. JCI Insight *8*, e165841. https://doi.org/10.1172/jci.insight.165841.
39. Lumpkin, C.J., Patel, H., Potts, G.K., Chaurasia, S., Gibilisco, L., Srivastava, G.P., Lee, J.Y., Brown, N.J., Amarante, P., Williams, J.D., et al. (2024). Broad proteomics analysis of seeding-induced aggregation of α-synuclein in M83 neurons reveals remodeling of proteostasis mechanisms that might contribute to Parkinson's disease pathogenesis. Mol. Brain *17*, 26. https://doi.org/10.1186/s13041-024-01099-1.
40. Aiken, J., and Holzbaur, E.L.F. (2024). Spastin locally amplifies microtubule dynamics to pattern the axon for presynaptic cargo delivery. Curr. Biol. *34*, 1687–1704.e8. https://doi.org/10.1016/j.cub.2024.03.010.
41. Murphy, D.D., Rueter, S.M., Trojanowski, J.Q., and Lee, V.M. (2000). Synucleins Are Developmentally Expressed, and α-Synuclein Regulates the Size of the Presynaptic Vesicular Pool in Primary Hippocampal Neurons. J. Neurosci. *20*, 3214–3220. https://doi.org/10.1523/JNEUROSCI.20-09-03214.2000.
42. Courte, J., Bousset, L., Boxberg, Y.V., Villard, C., Melki, R., and Peyrin, J.M. (2020). The expression level of alpha-synuclein in different neuronal populations is the primary determinant of its prion-like seeding. Sci. Rep. *10*, 4895. https://doi.org/10.1038/s41598-020-61757-x.
43. Dilsizoglu Senol, A., Samarani, M., Syan, S., Guardia, C.M., Nonaka, T., Liv, N., Latour-Lambert, P., Hasegawa, M., Klumperman, J., Bonifacino, J.S., and Zurzolo, C. (2021). α-Synuclein fibrils subvert lysosome structure and function for the propagation of protein misfolding between cells through tunneling nanotubes. PLoS Biol. *19*, e3001287. https://doi.org/10.1371/journal.pbio.3001287.
44. Bae, E.-J., Kim, D.-K., Kim, C., Mante, M., Adame, A., Rockenstein, E., Ulusoy, A., Klinkenberg, M., Jeong, G.R., Bae, J.R., et al. (2018). LRRK2 kinase regulates α-synuclein propagation via RAB35 phosphorylation. Nat. Commun. *9*, 3465. https://doi.org/10.1038/s41467-018-05958-z.
45. Henderson, M.X., Sengupta, M., McGeary, I., Zhang, B., Olufemi, M.F., Brown, H., Trojanowski, J.Q., and Lee, V.M.Y. (2019). LRRK2 inhibition does not impart protection from α-synuclein pathology and neuron death

in non-transgenic mice. Acta Neuropathol. Commun. *7*, 28. https://doi.org/10.1186/s40478-019-0679-5.

46. Van Der Perren, A., Cabezudo, D., Gelders, G., Peralta Ramos, J.M., Van Den Haute, C., Baekelandt, V., and Lobbestael, E. (2021). LRRK2 Ablation Attenuates Alpha-Synuclein–Induced Neuroinflammation Without Affecting Neurodegeneration or Neuropathology In Vivo. Neurotherapeutics *18*, 949–961. https://doi.org/10.1007/s13311-021-01007-8.
47. Palumbos, S.D., Popolow, J., Goldsmith, J., and Holzbaur, E.L.F. (2025). Autophagic stress activates distinct compensatory secretory pathways in neurons. Proc. Natl. Acad. Sci. USA *122*, e2421886122. https://doi.org/10.1073/pnas.2421886122.
48. Henderson, M.X., Sengupta, M., Trojanowski, J.Q., and Lee, V.M.Y. (2019). Alzheimer's disease tau is a prominent pathology in LRRK2 Parkinson's disease. Acta Neuropathol. Commun. *7*, 183. https://doi.org/10.1186/s40478-019-0836-x.
49. Sekiya, H., Franke, L., Hashimoto, Y., Takata, M., Nishida, K., Futamura, N., Hasegawa, K., Kowa, H., Ross, O.A., McLean, P.J., et al. (2025). Widespread distribution of α-synuclein oligomers in LRRK2-related Parkinson's disease. Acta Neuropathol. *149*, 42. https://doi.org/10.1007/s00401-025-02872-9.
50. Jensen, N.M., Vitic, Z., Antorini, M.R., Viftrup, T.B., Parkkinen, L., and Jensen, P.H. (2025). Abundant non-inclusion α-synuclein pathology in Lewy body-negative LRRK2-mutant cases. Acta Neuropathol. *149*, 41. https://doi.org/10.1007/s00401-025-02871-w.
51. Jensen, N.M., Fu, Y., Betzer, C., Li, H., Elfarrash, S., Shaib, A.H., Krah, D., Vitic, Z., Reimer, L., Gram, H., et al. (2024). MJF-14 proximity ligation assay detects early non-inclusion alpha-synuclein pathology with enhanced specificity and sensitivity. npj Parkinson's Dis. *10*, 227. https://doi.org/10.1038/s41531-024-00841-9.
52. Bonet-Ponce, L., Beilina, A., Williamson, C.D., Lindberg, E., Kluss, J.H., Saez-Atienzar, S., Landeck, N., Kumaran, R., Mamais, A., Bleck, C.K.E., et al. (2020). LRRK2 mediates tubulation and vesicle sorting from lysosomes. Sci. Adv. *6*, eabb2454. https://doi.org/10.1126/sciadv.abb2454.
53. Waschbüsch, D., Purlyte, E., Pal, P., McGrath, E., Alessi, D.R., and Khan, A.R. (2020). Structural Basis for Rab8a Recruitment of RILPL2 via LRRK2 Phosphorylation of Switch 2. Structure *28*, 406–417.e6. https://doi.org/10.1016/j.str.2020.01.005.
54. Cason, S.E., and Holzbaur, E.L.F. (2023). Axonal transport of autophagosomes is regulated by dynein activators JIP3/JIP4 and ARF/RAB GTPases. J. Cell Biol. *222*, e202301084. https://doi.org/10.1083/jcb.202301084.
55. Goldsmith, J., Ordureau, A., Harper, J.W., and Holzbaur, E.L.F. (2022). Brain-derived autophagosome profiling reveals the engulfment of nucleoid-enriched mitochondrial fragments by basal autophagy in neurons. Neuron *110*, 967–976.e8. https://doi.org/10.1016/j.neuron.2021.12.029.
56. Caputo, A., Liang, Y., Raabe, T.D., Lo, A., Horvath, M., Zhang, B., Brown, H.J., Stieber, A., and Luk, K.C. (2020). Snca-gfp knock-in mice reflect patterns of endogenous expression and pathological seeding. eNeuro *7*, 1–18. https://doi.org/10.1523/ENEURO.0007-20.2020.
57. Guedes-Dias, P., Nirschl, J.J., Abreu, N., Tokito, M.K., Janke, C., Magiera, M.M., and Holzbaur, E.L.F. (2019). Kinesin-3 Responds to Local Microtubule Dynamics to Target Synaptic Cargo Delivery to the Presynapse. Curr. Biol. *29*, 268–282.e8. https://doi.org/10.1016/j.cub.2018.11.065.
58. Pantazis, C.B., Yang, A., Lara, E., McDonough, J.A., Blauwendraat, C., Peng, L., Oguro, H., Kanaujiya, J., Zou, J., Sebesta, D., et al. (2022). A reference human induced pluripotent stem cell line for large-scale collaborative studies. Cell Stem Cell *29*, 1685–1702.e22. https://doi.org/10.1016/j.stem.2022.11.004.
59. Dou, D., Holzbaur, E.L.F., and Boecker, C.A. (2025). Protocol for live imaging of axonal transport in iPSC-derived iNeurons. STAR Protoc. *6*, 103556. https://doi.org/10.1016/j.xpro.2024.103556.
60. Fernandopulle, M.S., Prestil, R., Grunseich, C., Wang, C., Gan, L., and Ward, M.E. (2018). Transcription Factor-Mediated Differentiation of Human iPSCs into Neurons. Curr. Protoc. Cell Biol. *79*, e51. https://doi.org/10.1002/cpcb.51.
61. Boecker, C.A., Olenick, M.A., Gallagher, E.R., Ward, M.E., and Holzbaur, E.L.F. (2020). ToolBox: Live Imaging of intracellular organelle transport in induced pluripotent stem cell-derived neurons. Traffic *21*, 138–155. https://doi.org/10.1111/tra.12701.
62. Kaech, S., and Banker, G. (2006). Culturing hippocampal neurons. Nat. Protoc. *1*, 2406–2415. https://doi.org/10.1038/nprot.2006.356.
63. Dauer née Joppe, K., Tatenhorst, L., Caldi Gomes, L., Zhang, S., Parvaz, M., Carboni, E., Roser, A.E., El DeBakey, H., Bähr, M., Vogel-Mikuš, K., et al. (2021). Brain iron enrichment attenuates α-synuclein spreading after injection of preformed fibrils. J. Neurochem. *159*, 554–573. https://doi.org/10.1111/jnc.15461.
64. Berg, S., Kutra, D., Kroeger, T., Straehle, C.N., Kausler, B.X., Haubold, C., Schiegg, M., Ales, J., Beier, T., Rudy, M., et al. (2019). ilastik: interactive machine learning for (bio)image analysis. Nat. Methods *16*, 1226–1232. https://doi.org/10.1038/s41592-019-0582-9.

STAR★METHODS

KEY RESOURCES TABLE

REAGENT or RESOURCE	SOURCE	IDENTIFIER
Antibodies		
Anti-RAB10 antibody, Mouse Monoclonal	Nanotools	0680-100/Rab10-605B11; RRID: AB_2921226
Anti-RAB10 (phospho T73) antibody, Rabbit Monoclonal	Abcam	ab230261; RRID: AB_2811274
Anti-RAB12 antibody, Mouse Monoclonal	Santa Cruz Biotechnology	sc-515613; RRID: AB_3101762
Anti-RAB12 (phospho S106), Rabbit Monoclonal	Abcam	ab256487; RRID: AB_2884880
Anti-PPM1H antibody, Sheep Polyclonal	MRC PPU reagents and services, University of Dundee, Scotland	DA018, 3rd bleed; RRID: AB_2923281
Anti-LRRK2 antibody, Rabbit Monoclonal	Abcam	ab133474; RRID: AB_2713963
Anti-αSynuclein antibody, Rabbit Monoclonal	Cell Signaling	4179; RRID: AB_1904156
Anti-Rabbit IgG-IRDye 800CW, Donkey Polyclonal	Li-COR Biosciences	926-32213; RRID: AB_621848
Anti-Mouse IgG-IRDye 680RD, Donkey Polyclonal	Li-COR Biosciences	926-68073; RRID: AB_10954442
Anti-Sheep Alexa Fluor 680, Donkey Polyclonal	Thermo Fisher	A21102; RRID: AB_10374469
Anti-αSynuclein (phospho S129) antibody, Rabbit Monoclonal	Abcam	ab51253; RRID: AB_869973
Anti-αSynuclein (phospho S129) antibody, Mouse Monoclonal	BioLegend	825701; RRID: AB_2564891
Anti-LC3 antibody, Rabbit Polyclonal	Abcam	ab48394; RRID: AB_881433
Anti-GABARAP/L1/L2 antibody, Rabbit Monoclonal	Abcam	ab109364; RRID: AB_10861928
Anti-αSynuclein antibody, Mouse Monoclonal	BD	610787; RRID: AB_398108
Anti-Synapsin1/2 antibody, Rabbit Polyclonal	Synaptic Systems	106002; RRID: AB_887804
Anti-Bassoon antibody, Guinea Pig Monoclonal	Synaptic Systems	141318; RRID: AB_2927388
Anti-Homer1 antibody, Rabbit Polyclonal	Synaptic Systems	160003; RRID: AB_887730
Anti-MAP2 antibody, Mouse Monoclonal	Millipore	MAB3418; RRID: AB_94856
Anti-MAP2 antibody, Chicken Polyclonal	Abcam	ab5392; RRID: AB_2138153
Anti-Chicken Alexa Fluor 405, Goat Polyclonal	Thermo Fisher	A-48260; RRID: AB_2890271
Anti-Rabbit Alexa Fluor 488, Goat Polyclonal	Thermo Fisher	A-11034; RRID: AB_2576217
Anti-Mouse Alexa Fluor 488, Goat Polyclonal	Thermo Fisher	A-11001; RRID: AB_2534069
Anti-Mouse Alexa Fluor 594, Goat Polyclonal	Thermo Fisher	A-11005; RRID: AB_2534073

(*Continued on next page*)

Continued

REAGENT or RESOURCE	SOURCE	IDENTIFIER
Anti-Mouse Alexa Fluor 546, Goat Polyclonal	Thermo Fisher	A-11030; RRID: AB_2737024
Anti-Chicken Alexa Fluor 647, Goat Polyclonal	Thermo Fisher	A-21449; RRID: AB_2535866
Anti-Rabbit Alexa Fluor 647, Goat Polyclonal	Thermo Fisher	A-21245; RRID: AB_2535813
Chemicals, peptides, and recombinant proteins		
MLi-2	Tocris	5756
DMSO	AppliChem	A3672,0100
Poly-L-Lysine (mol wt 70,000–150,000)	Sigma-Aldrich	P1274
HBSS (10x)	Thermo Fisher	14185–052
1M HEPES	Thermo Fisher	15630–080
2.5% Trypsin	Thermo Fisher	15090–046
Minimum essential medium (MEM)	Thermo Fisher	11095–072
Horse serum (heat inactivated)	Thermo Fisher	16050–122
Sodium pyruvate	Thermo Fisher	11360–039
D-Glucose solution 45%	Sigma-Aldrich	G8769
GlutaMAX	Thermo Fisher	35050061
B27 Supplement	Thermo Fisher	17504–044
Neurobasal Medium	Thermo Fisher	21103–049
Penicillin-Streptomycin	Thermo Fisher	15140–122
Lipofectamine 2000 Transfection Reagent	Thermo Fisher	11668019
Matrigel Growth Factor Reduced	Corning	354230
Essential 8 Medium	Thermo Fisher	A1517001
ReLeSR	Stemcell Technologies	05872
Accutase	Sigma-Aldrich	A6964
ROCK Inhibitor Y-27632	Selleckchem	S1049
Knockout Serum Replacement	Thermo Fisher	10828010
DMEM/F-12, HEPES	Thermo Fisher	11330032
N2 Supplement	Thermo Fisher	17502048
Non-essential Amino Acids (NEAA)	Thermo Fisher	11140050
Doxycycline	Sigma-Aldrich	D9891
Poly-L-Ornithine	Sigma-Aldrich	P3655
BrainPhys Neuronal Medium	Stemcell Technologies	05790
Lipofectamine STEM Transfection Reagent	Thermo Fisher	STEM00003
Laminin	Corning	354232
BDNF	PeproTech	450–02
NT-3	PeproTech	450–03
Microcystin-LR	Sigma-Aldrich	475815
Halt Protease and Phosphatase Inhibitor Cocktail	Thermo Fisher	78442
Pepstatin A	Sigma-Aldrich	P5318
E64d	Sigma-Aldrich	E8640
5-Fluoro-2′-deoxyuridine	Sigma-Aldrich	F0503
Uridine	Sigma-Aldrich	U3003
EveryBlot Blocking Buffer	BioRad	12010020
Critical commercial assays		
BCA Protein Assay Kit	Thermo Fisher	23225
ZymoPURE II Plasmid Maxiprep Kit	ZymoResearch	D4203

(*Continued on next page*)

Continued

REAGENT or RESOURCE	SOURCE	IDENTIFIER
Experimental models: cell lines		
Human: KOLF2.1J WT iPSCs	B. Skarnes (Jackson Laboratories, Connecticut)	RRID: CVCL_B5P3
Human: KOLF2.1J LRRK2-R1441H iPSCs	B. Skarnes (Jackson Laboratories, Connecticut)	N/A
Human: KOLF2.1J PPM1H KO iPSCs	Dou et al.[13]	RRID: CVCL_C7TY
Experimental models: organisms/strains		
Mouse: LRRK2-G2019S knock-in	Taconic	13940
Mouse: C57BL/6NTac WT	Taconic	B6
Mouse: PPM1H knock-out	Taconic	TF3142
Recombinant DNA		
Plasmid: CMV mScarlet-LC3B	Modified from EGFP-LC3B (gift from T. Yoshimori, Osaka University, Japan)	Addgene plasmid #200431
Plasmid: PGK mCherry-LC3B	Modified from pLEX PGK mCherry-LC3B (gift from Michael Ward, NIH)	N/A
Plasmid: CMV SEP-LAMP1-RFP	Gift from J. Bonifacino (NIH)	Addgene plasmid #167970
Plasmid: CMV aSyn-EGFP	VectorBuilder, same linker as described in[56]	VB230227-1242vtx
Plasmid: PGK aSyn-EGFP	VectorBuilder, same linker as described in[56]	VB251105-1468fsr
Plasmid: PB-TO-hNGN2	Gift from iPSC Neurodegenerative Disease Initiative (iNDI) & Michael Ward	Addgene plasmid #172115
Plasmid: piggyBac™ transposase vector	Transposagen	N/A
Software and algorithms		
FIJI (Release 2.9.0)	NIH, USA	http://fiji.sc
Prism 10	GraphPad	https://www.graphpad.com/scientific-software/prism/
RStudio: Integrated Development for R (2022.07.0)	RStudio Team	http://www.rstudio.com/
R package: nlme	Pinheiro J, Bates D, R Core Team	http://CRAN.R-project.org/package=nlme
R package: lme4	Bates D, Mächler M, Bolker B, Walker S	https://cran.r-project.org/web/packages/lme4/index.html
MATLAB R2022a	MathWorks	https://www.mathworks.com/products/matlab.html
KymoSuite (custom MATLAB script)	Guedes-Dias et al.[57]	https://github.com/jnirschl/kinesin-3_guedes-dias_2018/tree/master/kymoSuite, https://zenodo.org/record/2530934
VisiView	Visitron	https://www.visitron.de/products/visiviewr-software.html
ZEN blue	Zeiss	https://www.zeiss.com/microscopy/en/products/software/zeiss-zen.html
Image Studio	LI-COR	https://www.licor.com/bio/image-studio/
Adobe Illustrator 2023	Adobe	https://www.adobe.com/products/illustrator.html
BioRender	BioRender	https://biorender.com/
Other		
35 mm #1.5 glass bottom imaging dishes	MatTek	P35G-1.5-20-C
12 mm #1.5 glass coverslips	R. Langenbrinck GmbH	01-0012/5
ProLong Gold Antifade Mountant	Thermo Fisher	P36930

EXPERIMENTAL MODEL AND STUDY PARTICIPANT DETAILS

Primary neuron culture

PPM1H KO mice (Taconic #TF3142) were provided by Dario Alessi, University of Dundee, and have been previously described.[33] A license for maintaining a colony of PPM1H KO mice was obtained from the manufacturer. All animal experiments were approved by the Lower Saxony State Office for Consumer Protection and Food Safety (LAVES) and complied with all relevant regulatory standards. Mouse cortices were dissected from littermate PPM1H$^{+/+}$, PPM1H$^{+/-}$, and PPM1H$^{-/-}$ embryos at day 15.5. The sex of the embryos was not determined; and thus sex-dependent differences in the observed phenotypes could not be evaluated. Upon sacrificing PPM1H KO embryos, tails were collected and used for genotyping. Cortical neurons were isolated by digestion with 0.25% trypsin and trituration through a small-bore serological pipette. Neurons were plated in attachment media (MEM supplemented with 10% horse serum, 33 mM D-glucose and 1 mM sodium pyruvate) on 35 mm glass-bottom imaging dishes (P35G-1.5-20-C; MatTek) for live-imaging experiments (200,000 neurons per dish), 24-well plates with 12 mm #1.5 coverslips for PFF experiments (100,000 neurons per well), or 6-well plates for biochemistry experiments (1,000,000 neurons per well). Attachment media was replaced with maintenance media (Neurobasal supplemented with 2% B-27, 33 mM D-glucose, 2 mM GlutaMAX, 100 U/mL penicillin and 100 mg/mL streptomycin) 3–5 h after plating. In imaging dishes and 6-well plates, 40% of the media was replaced with fresh maintenance media twice per week. Neurons in 24-well plates used for PFF experiments were fed by adding 10% maintenance media twice per week.

PiggyBac-mediated iPSC-derived neuron differentiation and iNeuron culture

KOLF2.1J-background WT, LRRK2-p.R1441H KI, and PPM1H KO iPSCs have been described and characterized previously.[13] KOLF2.1J-background iPSCs are genetically male and of European ancestry.[58] Cytogenetic analysis of G-banded metaphases cells showed a normal male karyotype (Cell Line Genetics). Mycoplasma testing was negative. iPSCs were cultured on plates coated with Growth Factor Reduced Matrigel (Corning) and fed daily with Essential 8 media. To stably express doxycycline-inducible hNGN2 using a PiggyBac delivery system, iPSCs were transfected with PB-TO-hNGN2 vector (gift from M. Ward, NIH, Maryland) in a 1:2 ratio (transposase:vector) using Lipofectamine Stem.[13,59] After 72 h, transfected iPSCs were selected for 48 h with 0.5 mg/mL puromycin. Differentiation of PB-TO-hNGN2 iPSCs into iNeurons was then performed using an established protocol.[13,59,60] In brief, iPSCs were passaged using Accutase and plated on Matrigel-coated dishes in induction media (DMEM/F12 supplemented with 1% N2-supplement, 1% NEAA, and 1% GlutaMAX, and containing 2 mg/mL doxycycline). After 72 h of doxycycline exposure, iNeurons were dissociated with Accutase and cryo-preserved in liquid N2.

Cryo-preserved, pre-differentiated iNeurons were thawed and plated on coverslips coated with poly-L-ornithine at a density of 200,000 neurons per well in 24-well plates. iNeurons were cultured in BrainPhys Neuronal Media (StemCell) supplemented with 2% B-27, 10 ng/mL BDNF (PeproTech), 10 ng/mL NT-3 (PeproTech), and 1 mg/mL laminin. Neurons were fed by adding 10% fresh media twice per week. 10 mM 5-Fluoro-20-deoxyuridine and 10 mM uridine were included at the time of plating to prevent survival of mitotic cells. These drugs were removed 24 h after plating. For each experimental condition, cells from at least two different batches of induction were used over three or more independent experimental cultures. Protocols for PiggyBac-mediated differentiation of iPSCs and culture of iNeurons can be found in a recently published protocol paper.[59]

METHOD DETAILS

Live-cell imaging

Live-cell imaging experiments were performed at the Live-Cell Imaging Facility of the Max Planck Institute for Multidisciplinary Sciences, Goettingen. Primary mouse cortical neurons were imaged at DIV8-9 in low fluorescence Hibernate E medium (Brain Bits) supplemented with 2% B27 and 2 mM GlutaMAX. iNeurons were imaged at DIV21-22 in low fluorescence Hibernate A medium (Brain Bits) supplemented with 2% B27, 10 ng/mL BDNF and 10 ng/mL NT-3. All live-cell imaging was conducted in an environmental chamber at 37°C. Time lapse series were recorded on a Visitron CSU-W1 Spinning Disk Confocal system with a Nikon Ti2 inverted microscope and a Prime BSI sCMOS camera controlled by VisiView software. Primary neurons expressing mScarlet-LC3B alone or co-expressing mScarlet-LC3B and aSyn-EGFP, as well as iNeurons co-expressing mCherry-LC3B and aSyn-EGFP, were imaged using a Plan Apochromat 60x 1.40 NA oil immersion objective. Primary neurons expressing SEP-LAMP1-RFP were imaged using an Apochromat 100x 1.49 NA oil immersion objective. Axons were identified based on morphological parameters.[61,62] For AV motility experiments, time lapse recordings were acquired at a frame rate of 1 frame/sec for 5 min in the mid-axon (>300 μm from the soma and >100 μm from the distal axon terminal). SEP-LAMP1-RFP recordings were acquired at a frame rate of 2 frames/sec for 5 min in the mid-axon. For analyzing the fraction of aSyn-EGFP-positive AVs, time lapse series were recorded at a frame rate of 1 frame/sec for 5 min in the proximal axon (<150 μm from the cell soma) and distal axon (region immediately proximal to the axon tip).

PFF assay

Purification of recombinant human aSyn and generation of aSyn PFFs was performed as previously described.[63] PFFs at a concentration of 25 μM were sonicated for 30 s using a Bandelin SonoPlus sonicator (10% power, 1 cycle) immediately before usage. PFFs were then diluted in media to 2x of their final concentration and added to cultured neurons by removing 50% of culture media from

each well and replacing it with an equal amount of PFF-containing media. For PBS control conditions, an equal volume of PBS was used instead of PFFs. For aSyn monomer control conditions, an equal concentration of monomer was used instead of PFFs. PFFs were added to DIV7 mouse cortical neurons at a final concentration of 0.5 μM and to DIV14 iNeurons at a final concentration of 0.25 or 0.5 μM. All experiments were performed using human aSyn PFFs. After adding PFFs, neurons were fed by adding 10% of fresh media twice per week. For MLi-2 experiments, mouse cortical neurons were treated with DMSO or 300 nM MLi-2 on DIV5 and fed with media containing DMSO or MLi-2 until fixation. On DIV21 (mouse cortical neurons) or DIV28/DIV35 (iNeurons), cells were fixed with 4% PFA and 4% sucrose at 37°C for 9 min. After three washes with PBS, cells were blocked/permeabilized for 1.5 h with PBS containing 5% normal goat serum, 1% BSA, and 0.1% Triton X-. Neurons were then incubated with primary antibodies diluted in blocking solution overnight at 4°C, washed three times with PBS, and incubated in secondary antibodies diluted in blocking solution for 1 h at RT. The following primary antibodies were used: Abcam EP1536Y Rabbit anti-pS129 alpha-synuclein (ab51253; 1:500), Millipore Mouse anti-MAP2 (MAB3418; 1:200). After three washes with PBS and nuclear counterstaining with DAPI, coverslips were mounted in ProLong Gold Antifade mountant. Immunofluorescently stained mouse cortical neurons were imaged on the Visitron CSU-W1 Spinning Disk confocal system described above using a 40x Plan Apochromat 0.95 NA air objective. Images were recorded as z-stacks with 400 nm step size. Images of pS129 aggregates within the soma were acquired as z-stacks with 300 nm step size using a 60x Plan Apochromat 1.40×NA oil immersion objective and 1.5× internal magnification. iNeurons were imaged on a Zeiss Axioplan 2 epifluorescence microscope controlled by ZEN blue software using a 20x Plan Apochromat 0.80 NA air objective and Zeiss Apotome 3.

In experiments assaying co-localization of pS129-positive aggregates with autophagosome markers, PFF-treated DIV14 primary cortical neurons were fixed and permeabilized for 8 min at −20°C using ice-cold methanol. After three washes with PBS, cells were blocked for 1.5 h with PBS containing 5% normal goat serum and 1% BSA. Following the staining protocol described above, neurons were incubated with the following primary antibodies: BioLegend Mouse anti-pS129 alpha-synuclein (#825701, 1:2000), Abcam Rabbit anti-LC3 (ab48394, 1:1000), Abcam Rabbit anti-GABARAP+GABARAPL1+ GABARAPL2 (ab109364, 1:200). Imaging was performed on the Visitron CSU-W1 Spinning Disk confocal system described above using a 100x Apochromat 1.49 NA oil objective; images were recorded as z-stacks with 300 nm step size.

ATTO 488-labeled PFF assay

ATTO 488-labeled PFFs were diluted to 25 μM with PBS and sonicated as described above. Labeled PFFs were then diluted in media to 1 μM and added to cultured mouse cortical neurons on DIV7 by removing 50% of culture media from each well and replacing it with an equal amount of PFF-containing media (final concentration: 0.5 μM). On DIV8, neurons were washed once with 1x Trypsin-EDTA diluted 1:10 in PBS for 30 s and once with PBS to remove extracellular PFFs, as described previously.[43] Cells were then fixed with 4% PFA and 4% sucrose and stained for MAP2 as described above. Stained neurons were imaged on the Visitron CSU-W1 Spinning Disk confocal system described above using a 100x Apochromat 1.49 NA oil immersion objective. Images were recorded as z-stacks with 300 nm step size.

Immunofluorescence

DIV28 iNeurons and DIV21 primary cortical neurons were fixed with 4% PFA and 4% sucrose at 37°C for 9 min. After three washes with PBS, cells were blocked/permeabilized for 1.5 h with PBS containing 5% normal goat serum, 1% BSA, and 0.1% Triton X-. Neurons were then incubated with primary antibodies diluted in blocking solution overnight at 4°C, washed three times with PBS, and incubated with secondary antibodies diluted in blocking solution for 1 h at RT. The following primary antibodies were used: Synaptic Systems Rabbit anti-synapsin (#106002; 1:500), BD Mouse anti-aSyn (#610787; 1:1000), Abcam Chicken anti-MAP2 (ab5392; 1:5000), Synaptic Systems Guinea Pig anti-bassoon (#141318; 1:5000), Synaptic Systems Rabbit anti-homer1 (#160003; 1:1000. After three washes with PBS, coverslips were mounted in ProLong Gold Antifade mountant. Primary neurons and iNeurons stained for synapsin, aSyn, and MAP2 were imaged on the Visitron CSU-W1 Spinning Disk confocal system described above using a 100x Apochromat 1.49 NA oil objective; images were recorded as z-stacks with 300 nm step size. Primary neurons stained for bassoon, homer1, and MAP2 were imaged on a Zeiss LSM800 laser scanning confocal microscope using a 63x Plan Apochromat 1.40 NA oil objective and ZEN software (Zeiss) in Airyscan mode.

Immunoblotting

Neurons were washed twice with ice-cold PBS and lysed with RIPA buffer (50 mM Tris-HCl, 150 mM NaCl, 0.1% Triton X-100, 0.5% deoxycholate, 0.1% SDS, 2x Halt Protease and Phosphatase inhibitor, 2mg/mL microcystin-LR). Samples were centrifuged for 10 min at 16,200 g, and protein concentration of the supernatant was determined by BCA assay. Proteins were resolved on 8% (LRRK2), 10% (PPM1H), or 15% (RAB proteins) acrylamide gels. Proteins were transferred to Immobilon-FL PVDF membranes (Millipore) using a wet blot transfer system. For PPM1H blots, membranes were then stained for total protein using LI-COR Revert 700 Total Protein Stain. Following imaging of total protein stain, membranes were de-stained, blocked for 5 min with Bio-Rad EveryBlot blocking buffer, and incubated with primary antibody diluted in EveryBlot for 90 min at room temperature. For pT73 RAB10, total RAB10, aSyn, pS106 RAB12, total RAB12, and LRRK2 blots, membranes were blocked for 5 min with EveryBlot after protein transfer and then incubated with primary antibody diluted in EveryBlot at 4°C overnight. After three washes with TBS (50 mM Tris-HCl [pH 7.4], 274 mM NaCl, 9 mM KCl) with 0.1% Tween 20, membranes were incubated with secondary antibodies diluted in EveryBlot with

0.01% SDS for 1 h at RT. Following three more washes with TBS with 0.1% Tween 20, membranes were imaged using an Odyssey CLx Infrared Imaging System (LI-COR). Western blots were analyzed with Image Studio Software (LI-COR).

QUANTIFICATION AND STATISTICAL ANALYSIS

AV motility

Kymographs of LC3+ AVs were generated with the Multiple Kymograph plugin for FIJI using a line width of 5 pixels. Vesicle tracks were traced manually with a custom MATLAB GUI (KymoSuite). Motile AVs were scored as anterograde (net displacement >10 μm in the anterograde direction within 5 min), retrograde (net displacement >10 μm in the retrograde direction) or bidirectional (net displacement <10 μm, but total displacement >10 μm). AVs with net and total displacement <10 μm were scored as stationary. A pause was defined as a single or consecutive instantaneous velocity value of <0.083 μm/s. Stationary AVs were excluded from the quantification of pause number, pause duration, and directional reversals. Quantification of the fraction of time paused included all (motile and stationary) AVs. All analyses were performed by a blinded investigator.

Fraction of aSyn-EGFP-positive AVs and number of aSyn-EGFP puncta

Time lapse series were recorded in the proximal axon (<150 μm from the cell soma) and distal axon (region immediately proximal to the axon tip). Kymographs were generated using the Multiple Kymograph plugin for FIJI as described above. For quantification of the fraction of aSyn-EGFP-positive AVs, traces were counted first in the aSyn-EGFP kymograph, then in the mScarlet-LC3 (primary neurons) or mCherry-LC3 (iNeurons) kymograph by a blinded investigator. For quantification of the number of aSyn-EGFP puncta, the number of aSyn-EGFP-positive puncta present in the first frame of the time lapse acquisition was counted and normalized to 100 μm of axonal length.

Lysosome acidification

Time lapse series were recorded in the mid-axon. Kymographs were generated using the Multiple Kymograph plugin for FIJI. Traces of LAMP1 vesicles were counted first in the SEP, then in the RFP kymograph by a blinded investigator.

PFF assay

To quantify the area of pS129 aSyn and MAP2 signal, max projections of each channel were made for each image. Both pS129 aSyn and MAP2 signal were thresholded and binarized in an unbiased manner using ilastik segmentation, a machine-learning based approach to image segmentation.[64] The binarized images were used to quantify pS129-positive area, pS129-positive aggregate number and size, and MAP2 area using the measure function in FIJI. For quantification of pS129-positive aggregates in the soma the ''Analyze Particles'' command was applied to a manually selected region of interest outlining the cell soma.

Presynapse and synapse number

To quantify the number of presynapses (defined as the number of synapsin puncta overlapping with MAP2 signal) in iNeurons and primary mouse cortical neurons, max projections of the synapsin and MAP2 channels were created and thresholded using ilastik segmentation. Using the ''AND'' function of the image calculator in FIJI, the binarized images were next processed to show only synapsin signal overlapping with MAP2 signal. The analyze particle function (size: 10 pixel^2 – infinity) and the measure function in FIJI were then used to quantify the number of presynaptic puncta and MAP2 area, respectively.

To quantify the number of synapses (defined by colocalization of presynaptic and postsynaptic markers) in primary mouse cortical neurons, ilastik was trained to generate segmented images for neurons of all genotypes in an automated and unbiased manner. The segmented images were then analyzed using Fiji. The number of synapses was determined by identifying double-positive puncta (homer1: postsynaptic marker and bassoon: presynaptic marker) using the ''AND'' function of the Image Calculator and the ''Analyze Particles'' command within the software.

Tagged PFF assay

To quantify intracellular uptake of ATTO 488-labeled PFFs, max projections of each channel were generated. Somata of the imaged cells were outlined manually to create regions of interest by a blinded investigator. ATTO 488 signal was thresholded and binarized using ilastik. Binary images and max projections were overlayed with the created regions of interest and analyzed with the FIJI measure tool to analyze the ATTO 488-positive area and the integrated density, respectively.

Statistical analysis

Figure legends contain descriptions of the statistical test(s) used, specific *p*-values, sample size, and dispersion/precision measurements. For AV transport experiments, statistical analysis of AV directionality was performed by two-way ANOVA with Sidak's test for multiple comparisons using GraphPad Prism 10. For other transport parameters, RStudio version 2022.07.0 was used to perform a generalized linear mixed model (GLMM; R package ''lme4''). The genotype (or, in MLi-2 experiments, the treatment condition) was treated as the fixed effect. The independent experiment/culture and the neuron being recorded from were treated as nested random effects, with the neuron nested within the experiment. Specific models were selected as previously described, based on the

distribution of each dataset[13]. In detail, the following models were used: for fraction of time paused, GLMM (binomial family, with the ''weights'' argument for total time); for pause number, GLMM (Poisson family); for pause duration, GLMM (gamma family, log link function); for reversals, GLMM (Poisson family); for Δ run length, GLMM (gamma family, log link function, with transformation to remove zero values with added constants). Statistical analysis of the fraction of AVs positive for aSyn-EGFP, number of aSyn-EGFP positive puncta, pS129 area, MAP2 area, pS129 aggregate size, pS129 aggregate number, pS129 aggregate size in the soma, number of synapses, as well as area and integrated density of internalized ATTO 488-labeled PFFs was performed by a linear mixed effects model (LME; R package ''nlme'') in RStudio. The genotype was treated as the fixed effect. For experiments in primary mouse cortical neurons, the independent experiment/culture and the individual embryo from which neurons were obtained were treated as nested random effects, with the embryo nested within the experiment. For experiments in iPSC-derived iNeurons, the independent experiment/culture was treated as the random effect.